CrossMark

Reflection and transmission of a Kelvin–Helmholtz wave incident on a shock in a jet

Matteo Mancinelli[1,2,†], Eduardo Martini[1,3], Vincent Jaunet[1], Peter Jordan[1], Aaron Towne[4] and Yves Gervais[1]

[1]Département Fluides Thermique et Combustion, Institut Pprime - CNRS-Université de Poitiers-ENSMA, 11 Boulevard Marie et Pierre Curie, 86962 Chasseneuil-du-Poitou, France

[2]Dipartimento di Ingegneria, Università degli Studi Roma Tre, Via della Vasca Navale 79, 00146 Rome, Italy

[3]Direction des Applications Militaires, CEA-Cesta, 15 Avenue des Sablières, 33114 Le Barp, France

[4]Department of Mechanical Engineering, University of Michigan, 2350 Hayward Street, Ann Arbor, MI 48109, USA

Screech tones in supersonic jets are underpinned by resonance between downstream-travelling Kelvin–Helmholtz waves and upstream-travelling acoustic waves. Specifically, recent works suggest that the relevant acoustic waves are guided within the jet and are described by a discrete mode of the linearised Euler equations. However, the reflection mechanism that converts downstream-travelling waves into upstream-travelling waves, and *vice versa*, has not been thoroughly addressed, leading to missing physics within most resonance models. In this work, we investigate the reflection and transmission of waves generated by the interaction between a Kelvin–Helmholtz wave and a normal shock in an under-expanded jet using a mode-matching approach. Both vortex-sheet and finite-thickness shear-layer models are explored, quantifying the impact of the shear layer in the reflection process. This approach could enable more quantitative predictions of resonance phenomena in jets and other fluid systems.

1. Introduction

Shock-containing shear flows involve a rich variety of phenomena including shock–turbulence interaction (STI). In free shear layers, STI leads to an increase in

† Email address for correspondence: matteo.mancinelli@uniroma3.it

turbulence levels and mixing downstream of the shock (Génin & Menon 2010). In wall-bounded flows, in addition to the enhancement of turbulence, STI may also be accompanied by boundary layer separation and the formation of a separation bubble (Delery 1983; Dolling 2001; Clemens & Narayanaswamy 2014). The STI is also an important feature of supersonic combustion in scramjets (Yang, Kubota & Zukoski 1993). In imperfectly expanded propulsive jets, STI underpins the generation of broad-band shock associated noise (Tanna 1977; Tam & Tanna 1982) and screech (Powell 1953; Tam, Seiner & Yu 1986; Raman 1999; Edgington-Mitchell 2019).

Linear theory has been widely used to study the interaction between disturbance fields and shocks. Ribner (1954) considered the interaction between a vorticity wave and a normal shock. The analysis was later extended to consider STI, where a homogeneous turbulence was modelled as a superposition of Fourier vorticity waves (Ribner 1955). Moore (1954) considered the interaction between sound waves and an oblique shock, and this work was extended by Mahesh *et al.* (1995) to study an isotropic field of acoustic disturbances interacting with a shock. Later, Mahesh, Lele & Moin (1997) considered the influence of entropy fluctuations on STI as well and Buttsworth (1996) derived expressions for shock-induced vorticity, useful for the estimation of mixing enhancement. The foregoing studies were all based on solution of the Rankine–Hugoniot relations. The unsteady STI was converted into an equivalent steady-flow problem which did not consider the reflection process associated with the incident turbulent disturbance but only the transmission mechanism through the shock wave. A review of these studies and others has been compiled by Andreopoulos, Agui & Briassulis (2000). More recently, Kitamura *et al.* (2016) used rapid distortion theory to study the interaction between homogeneous isotropic turbulence and a shock wave, and Chen & Donzis (2019) considered STI at high turbulence intensities. Similarly to the works reported above, the authors mainly focused on the turbulence amplification and modification of the turbulence length scales downstream of the shock.

The reflection and transmission of acoustic, vorticity and entropy waves within a convergent–divergent nozzle with and without a shock was studied by Marble & Candel (1977). The study focused on compact disturbances, that is, with wavelengths larger than the nozzle length, thus limiting the application to low frequencies. The inclusion of non-compactness effects was considered by Stow, Dowling & Hynes (2002), who provided a first-order correction for the phase of the reflection coefficient for higher frequencies. The correction was extended to the transmission coefficient also by Goh & Morgans (2011) and a further development was carried out by Duran & Moreau (2013) and Duran & Morgans (2015), who extended the high-frequency correction to the amplitude of the reflection and transmission coefficients in the case of planar and circumferential incident waves, respectively. All of these works were motivated by the problem of combustion noise and the role the reflected waves play on the onset of thermo-acoustic instability in the combustion chamber of the burner–turbine–nozzle configuration of an aero-engine.

The problem we consider is motivated by the sound generated by imperfectly expanded, supersonic jets and, in particular, the phenomenon known as screech, a mechanistic explanation for which was first provided by Powell (1953). The mechanism involves turbulent structures that are convected through the shock-cell structure; this STI results in the generation of upstream-travelling sound waves. According to Powell's phenomenological description, when the phases of the upstream-travelling sound waves and downstream-travelling turbulent structures are suitably matched, at the jet exit plane and at the STI locations, resonance may occur. The downstream-travelling turbulent structures considered important for screech are what are often referred to as coherent structures.

A large body of recent work has shown how coherent structures in turbulent jets, and the sound they produce, can be modelled using linear theory (Jordan & Colonius 2013; Schmidt *et al.* 2017; Towne, Schmidt & Colonius 2018; Cavalieri, Jordan & Lesshafft 2019; Lesshafft *et al.* 2019; Nogueira *et al.* 2019; Edgington-Mitchell *et al.* 2021*a*). As shown in these studies, downstream-travelling coherent structures are largely underpinned by Kelvin–Helmholtz (K–H) instability. Powell (1953) assumed that the upstream-travelling waves responsible for the feedback mechanism in screech generation were free-stream acoustic waves, but this has been recently questioned. Shen & Tam (2002) suggested that the upstream-travelling disturbance might comprise a family of guided jet modes, first discussed by Tam & Hu (1989). This hypothesis has been recently confirmed in studies by Gojon, Bogey & Mihaescu (2018) and Edgington-Mitchell *et al.* (2018), and a simplified screech-tone prediction model based on this idea has been developed and validated by Mancinelli *et al.* (2019*a*). In the simplest formulation of the screech-tone model, the spatial growth of the K–H mode is ignored, and a phase-matching criterion is sufficient to provide a reasonable prediction of screech-tone frequencies. A similar resonant mechanism was proposed for subsonic compressible jets (Towne *et al.* 2017), cavity flows (Rossiter 1964; Rowley, Colonius & Basu 2002) and impinging jets (Tam & Ahuja 1990; Bogey & Gojon 2017). The reflection of waves is implicitly considered in all these mechanisms, but it is rarely studied in detail. In more complete screech-frequency prediction models (Mancinelli *et al.* 2019*b*, 2021), where the spatial growth rates of the upstream- and downstream-travelling waves are included, knowledge of the reflection coefficients in the jet exit plane and at the location of STI is required.

In this paper, we investigate the interaction between a downstream-travelling K–H wave and a normal shock and compute the amplitude and phase of the reflected upstream-travelling guided wave active in the screech loop using a mode-matching approach. We consider vortex-sheet (V-S) and finite-thickness (F-T) flow models, which elucidate the role of shear in the reflection and transmission processes. The efficiency of the mode-matching technique in the presence of a discontinuity, as is the shock in the flow we consider herein, has been already shown by Gabard & Astley (2008) for the estimation of the sound attenuation in a lined duct. More recently, a mode-matching approach has been used by Dai (2020, 2021) to calculate the reflection and transmission coefficients in a duct flow in the presence of a cavity. Consistent with these works, we use linear theory to describe the flow dynamics upstream and downstream of the shock and then match the solutions across the discontinuity.

The paper is organised as follows. The general modelling framework, including the jet models adopted and the mode-matching approach used to calculate the reflection and transmission coefficients, is presented in § 2. Results involving the reflection-coefficient calculation, its dependence on the frequency and jet-flow conditions and the reflected and transmitted pressure fields are presented and discussed in § 3. The paper closes with concluding remarks in § 4.

2. Modelling framework

We here present the shock and jet-dynamics modelling and the procedure adopted to calculate the reflection and transmission coefficients. We consider an axisymmetric, shock-containing supersonic jet. It is known that the organised structure of the jet plume of imperfectly expanded supersonic jets is shaped by oblique shocks and expansion waves (see the many flow visualisations presented in Powell 1953; Powell, Umeda & Ishii 1992; Panda 1999; Mercier, Castelain & Bailly 2017). Normal shocks are, however, found in the form of Mach disks for highly imperfectly expanded jets and often encountered in the
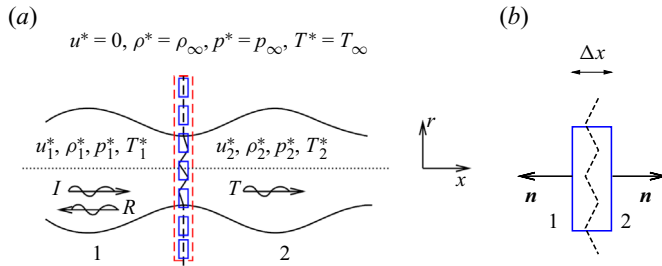
M. Mancinelli, E. Martini, V. Jaunet, P. Jordan, A. Towne and Y. Gervais

Figure 1. Schematic representation of the jet model: (*a*) sketch of the shock-containing jet, (*b*) control volume representation with identification of the normal to the inlet and outlet surfaces.

jet plume of convergent–divergent nozzles and impinging jets (Edgington-Mitchell 2019). Despite many years of research activity (see the many works by Powell 1953; Tam & Tanna 1982; Suzuki & Lele 2003; Lele 2005; Edgington-Mitchell *et al.* 2021*b*), a clear picture of the way by which instability waves interact with shock cells to generate screech is still far from being reached. With the aim of keeping the model as simple as possible and in the absence of a clear and unambiguous description of the interaction between instability and shock waves, the shock is herein assumed to be normal, thus allowing the use of the locally parallel-flow assumption both upstream and downstream of the shock. This assumption implies that the linear response to shock oscillations induced by the incoming instability wave, which is a typical non-parallel feature, is not considered. A sketch of the shock-containing jet and the cylindrical reference system used in this paper are depicted in figure 1. We consider a K–H wave with unitary amplitude, $I = 1$, incident to a shock. The interaction of the incoming wave with the shock generates a collection of reflected and transmitted modes upstream and downstream of the shock, respectively. The sections upstream and downstream of the shock are hereinafter denoted 1 and 2 and the reflection and transmission coefficients of each wave moving away from the shock are indicated with R_{n_R} and T_{n_T}, respectively. The state vector is $\boldsymbol{q}^* = \{\rho^*, u_x^*, u_r^*, u_\theta^*, T^*, p^*\}$, where ρ is the flow density, u the velocity, T the temperature and p the pressure. The flow variables are normalised by the nozzle diameter D and the ambient density and speed of sound ρ_∞ and c_∞, respectively, thus leading to a non-dimensional state vector $\boldsymbol{q}$.

2.1. *Shock model*

The flow regions upstream and downstream of the shock are well described by a locally parallel model. In order to connect these two regions, we impose the conservation laws of mass, momentum and energy through the shock. This is done by dividing the shock into infinitesimal control volumes dV of length $\Delta x \to 0$ such that the flux terms through the top and bottom surfaces are zero (see figure 1) and enforcing mass, momentum and energy conservation for the control volume, leading to the system of equations

$$\left.\begin{aligned}
\int_{S_1} \rho^* \boldsymbol{u}^* \cdot \boldsymbol{n} \, dS + \int_{S_2} \rho^* \boldsymbol{u}^* \cdot \boldsymbol{n} \, dS = 0, \\
\int_{S_1} \rho^* \boldsymbol{u}^* \left(\boldsymbol{u}^* \cdot \boldsymbol{n}\right) dS + \int_{S_1} p^* \boldsymbol{n} \, dS + \int_{S_2} \rho^* \boldsymbol{u}^* \left(\boldsymbol{u}^* \cdot \boldsymbol{n}\right) dS - \int_{S_2} p^* \boldsymbol{n} \, dS = 0, \\
\int_{S_1} \rho^* e^* \boldsymbol{u}^* \cdot \boldsymbol{n} \, dS + \int_{S_2} \rho^* e^* \boldsymbol{u}^* \cdot \boldsymbol{n} \, dS = 0,
\end{aligned}\right\} \quad (2.1a\text{-}c)$$

954 A9-4

where $e^* = h^* + 0.5(u_x^{*2} + u_r^{*2} + u_\theta^{*2})$ is the total specific energy with the enthalpy expressed as $h^* = c_p T^*$, c_p is the specific heat capacity, S is the control volume surface and n the normal to the surface. Normalising the flow variables, performing the Reynolds decomposition,

$$q(x, r, \theta, t) = \bar{q}(r) + q'(x, r, \theta, t), \tag{2.2}$$

and substituting into (2.1*a*), removing the mean and linearising, the linearised jump equations for the shock become

$$\left.\begin{aligned}
\bar{u}_{1x}\rho_1 + \bar{\rho}_1 u_{1x} &= \bar{u}_{2x}\rho_2 + \bar{\rho}_2 u_{2x}, \\
p_1 + 2\bar{\rho}_1\bar{u}_{1x}u_{1x} + \bar{u}_{1x}^2\rho_1 &= p_2 + 2\bar{\rho}_2\bar{u}_{2x}u_{2x} + \bar{u}_{2x}^2\rho_2, \\
u_{1r} &= u_{2r}, \\
u_{1\theta} &= u_{2\theta}, \\
T_1 + \bar{u}_{1x}u_{1x} &= T_2 + \bar{u}_{2x}u_{2x},
\end{aligned}\right\} \tag{2.3a–e}$$

where we removed the primes from the fluctuating variables for notational simplicity. We note that the adiabatic relation between the thermodynamic variables is implicit in the linearised operator. The perturbations upstream and downstream of the shock are modelled using the normal mode ansatz

$$q'(x, r, \theta, t) = \hat{q}(r)\exp(\mathrm{i}(kx + m\theta - \omega t)), \tag{2.4}$$

where k is the wavenumber along the axial direction, m is the azimuthal order and $\omega = 2\pi St M_a$ is a non-dimensional frequency, with $St = fD/U_j$ the nozzle-diameter-based Strouhal number, $M_a = U_j/c_\infty$ the acoustic Mach number, f the frequency, D the nozzle diameter and U_j the fully expanded jet velocity. Considering that the only incident wave is the K–H wave, the system of (2.3*a*) can be written in a compact form as follows:

$$\boldsymbol{A}_1\left(I\hat{q}_{1I} + \sum_{n_R=1}^{\infty} R_{n_R}\hat{q}_{1R,n_R}\right) = \boldsymbol{A}_2 \sum_{n_T=1}^{\infty} T_{n_T}\hat{q}_{2T,n_T}, \tag{2.5}$$

where $\hat{q}_{1I}$, $\hat{q}_{1R,n_R}$ and $\hat{q}_{2T,n_T}$ are the incident, reflected and transmitted waves moving upstream and downstream of the shock, respectively, and

$$\boldsymbol{A}_1 = \begin{bmatrix} \bar{u}_{1x} & \bar{\rho}_1 & 0 & 0 & 0 & 0 \\ \bar{u}_{1x}^2 & 2\bar{\rho}_1\bar{u}_{1x} & 0 & 0 & 0 & 1 \\ 0 & 0 & 1 & 0 & 0 & 0 \\ 0 & 0 & 0 & 1 & 0 & 0 \\ 0 & \bar{u}_{1x} & 0 & 0 & 1 & 0 \end{bmatrix}, \quad \boldsymbol{A}_2 = \begin{bmatrix} \bar{u}_{2x} & \bar{\rho}_2 & 0 & 0 & 0 & 0 \\ \bar{u}_{2x}^2 & 2\bar{\rho}_2\bar{u}_{2x} & 0 & 0 & 0 & 1 \\ 0 & 0 & 1 & 0 & 0 & 0 \\ 0 & 0 & 0 & 1 & 0 & 0 \\ 0 & \bar{u}_{2x} & 0 & 0 & 1 & 0 \end{bmatrix} \tag{2.6a,b}$$

are matrices containing information about the mean flow upstream and downstream of the shock. The vector of eigenfunctions $\hat{q}_{1I}$, $\hat{q}_{1R,n_R}$ and $\hat{q}_{2T,n_T}$ are computed using either a V-S or F-T model (see § 2.3). The procedure used to ascertain whether a wave is reflected or transmitted is described in § 2.3.3.

2.2. *Reflection- and transmission-coefficient calculation*

Equation (2.5) is exact if a complete basis of jet modes is considered. In order to estimate the reflection- and transmission-coefficient values, we truncate the sum to a finite number

of modes N_R and N_T and we introduce an error density $\epsilon(r)$ for each conservation equation. Equation (2.5) can then be written as

$$
A_1 \left(I\hat{q}_{1I} + \sum_{n_R=1}^{N_R} R_{n_R}\hat{q}_{1R,n_R} \right) - A_2 \sum_{n_T=1}^{N_T} T_{n_T}\hat{q}_{2T,n_T} = \epsilon,
\tag{2.7}
$$

where $\epsilon(r)$ is the error density vector and $\epsilon \to 0$ if the number of modes N_R and $N_T \to \infty$. The reflection and transmission coefficients R_{n_R} and T_{n_T} associated with each mode are estimated by a least-mean-square minimisation of the error densities, formalised as

$$
[R_{opt,n_R}, T_{opt,n_T}] = \min_{R_{n_R},T_{n_T} \in \mathcal{C}} \underbrace{\int_0^\infty |\epsilon^2(r)| \, dr}_{F}.
\tag{2.8}
$$

The objective function F corresponds to the sum of the absolute value of the squared error densities associated with each conservation equation integrated along the radial direction. To solve the minimisation problem in (2.8), we write (2.7) in a matrix form

$$
\begin{bmatrix} A_1\hat{Q}_{1R} & -A_2\hat{Q}_{2T} \end{bmatrix} \begin{Bmatrix} R \\ T \end{Bmatrix} = -IA_1\hat{q}_{1I} + \epsilon,
\tag{2.9}
$$

where $\hat{Q}_{1R} = [\hat{q}_{1R,1}, \ldots, \hat{q}_{1R,N_R}]$ and $\hat{Q}_{2T} = [\hat{q}_{2T,1}, \ldots, \hat{q}_{2T,N_T}]$ are the matrices of the eigenfunctions and R and T are the vectors of the reflection and transmission coefficients, respectively. We then define

$$
\begin{Bmatrix} R \\ T \end{Bmatrix} = X, \quad \begin{bmatrix} A_1\hat{Q}_{1R} & -A_2\hat{Q}_{2T} \end{bmatrix} = B, \quad y = A_1\hat{q}_{1I}I,
\tag{2.10}
$$

so that (2.9) can be written in the compact form $\epsilon = BX + y$. The solution of (2.8) is obtained by finding the stationary point of F by setting its gradient to zero

$$
\frac{dF}{dX} = \frac{d\left(\epsilon^T W\epsilon\right)}{dX} = B^T WBX + B^T Wy = 0,
\tag{2.11}
$$

which leads to

$$
X = -\left(B^T WB\right)^{-1} B^T Wy,
\tag{2.12}
$$

where $B|_W^+ = (B^T WB)^{-1}B^T W$ is the weighted pseudo-inverse matrix and W is a diagonal matrix of elements dr.

2.3. *Jet models*

We here present a local description of the jet dynamics using the parallel-flow linear stability theory. This theory is applied to two different models: a F-T flow model and a simplified cylindrical vortex sheet. Both are governed by the linearised Euler equations (LEE) (see Appendix A).

2.3.1. *Finite-thickness model*

Writing the LEE exclusively in terms of pressure, the compressible Rayleigh equation (Schmid & Henningson 2001)

$$\frac{\partial^2 \hat{p}}{\partial r^2} + \left(\frac{1}{r} - \frac{2k}{\bar{u}_x k - \omega} \frac{\partial \bar{u}_x}{\partial r} - \frac{\gamma - 1}{\gamma \bar{\rho}} \frac{\partial \bar{\rho}}{\partial r} + \frac{1}{\gamma \bar{T}} \frac{\partial \bar{T}}{\partial r} \right) \frac{\partial \hat{p}}{\partial r}$$

$$- \left(k^2 + \frac{m^2}{r^2} - \frac{(\bar{u}_x k - \omega)^2}{(\gamma - 1) \bar{T}} \right) \hat{p} = 0, \tag{2.13}$$

is obtained, where γ is the specific heat ratio for a perfect gas. The solution of the linear stability problem is obtained by specifying a real or complex frequency ω and solving the resulting augmented eigenvalue problem $k = k(\omega)$, with $\hat{p}(r)$ the associated pressure eigenfunction. The eigenvalue problem is solved numerically by discretising (2.13) in the radial direction using the Chebyshev polynomials and by imposing Dirichlet boundary conditions at the domain boundaries. A mapping function proposed by Lesshafft & Huerre (2007) is used to non-uniformly distribute the 500 grid points to efficiently resolve the shear layer of the jet and to ensure convergence of the computed eigenmodes. The eigenfunctions $\hat{u}_i$, $\hat{\rho}$ and $\hat{T}$ are calculated from the knowledge of $\hat{p}$ (see Appendix A). The eigenfunctions are normalised such that $\angle \hat{p}(r) = 0$ for $r = 0$ and to have unitary energy norm, which, following Chu (1965) and Hanifi, Schmid & Henningson (1996), is defined as

$$E = \frac{1}{2} \int_0^{2\pi} \int_0^\infty \left(\bar{\rho} \left(|\widehat{u_x}|^2 + |\widehat{u_r}|^2 + |\widehat{u_\theta}|^2 \right) + \frac{\gamma - 1}{\gamma} \frac{\bar{T}}{\bar{\rho}} |\hat{\rho}|^2 + \frac{\bar{\rho}}{\gamma \bar{T}} |\hat{T}|^2 \right) r \mathrm{d}r \, \mathrm{d}\theta. \tag{2.14}$$

The derivation of the energy norm is provided in Appendix B.

2.3.2. *Vortex-sheet model*

The V-S model is an inviscid idealisation of the jet where the infinitely thin V-S separates the interior flow and the outer quiescent fluid, resulting in a jet with a mean top-hat profile. The V-S was used by Lessen, Fox & Zien (1965) and Michalke (1970) to study the stability properties of a compressible jet. We recently showed that the standard V-S model for free jets, which was used in the previous studies, does not support free-stream acoustic waves as discrete modes, as required for the mode-matching procedure. To obtain a discrete representation of free-stream acoustic modes, we use the dispersion relation of a confined jet with the radial distance of the boundary (r_{MAX}) sufficiently distant from the jet in order to recover the same dynamical properties of a free jet. The analysis of this surrogate problem allowed us to include the free-stream acoustic modes in the description of the jet dynamics (for more details the reader can refer to Mancinelli *et al.* 2022). We herein use this confined version of the V-S, whose dispersion relation $D(k, \omega; M_a, T, m, r_{MAX}) = 0$ is,

$$\frac{1}{\left(1 - \frac{k M_a}{\omega} \right)^2} + \frac{1}{T} \frac{I_m \left(\frac{\gamma_i}{2} \right)}{K_m \left(\frac{\gamma_o}{2} \right) - z I_m \left(\frac{\gamma_o}{2} \right)}$$

$$\frac{\frac{\gamma_o}{2} K_{m-1} \left(\frac{\gamma_o}{2} \right) + m K_m \left(\frac{\gamma_o}{2} \right) + z \left(\frac{\gamma_o}{2} I_{m-1} \left(\frac{\gamma_o}{2} \right) - m I_m \left(\frac{\gamma_o}{2} \right) \right)}{\frac{\gamma_i}{2} I_{m-1} \left(\frac{\gamma_i}{2} \right) - m I_m \left(\frac{\gamma_i}{2} \right)} = 0, \tag{2.15}$$

with

$$
\left.\begin{aligned}
\gamma_i &= \sqrt{k^2 - \frac{1}{T}(\omega - M_a k)^2}, \\
\gamma_o &= \sqrt{k^2 - \omega^2},
\end{aligned}\right\}
\tag{2.16a}
$$

where I and K are modified Bessel functions of the first and second kinds, respectively, $T = T_j/T_\infty$ is the jet-to-ambient temperature ratio such that the relation between the jet and the acoustic Mach numbers is $M_a = M_j\sqrt{T}$ and $z = K_m(\gamma_o r_{MAX})/I_m(\gamma_o r_{MAX})$. The branch cut in the square root of (2.16) is chosen such that $-\pi/2 \leq \arg(\gamma_{i,o}) < p/2$. The dispersion relation in (2.15) for a confined jet differs from the unconfined one for a free jet in the additional terms containing $z(r_{MAX})$. Following Mancinelli *et al.* (2022), we herein use $r_{MAX} = 100$ in order to avoid any effect of the boundary on the eigenmodes. Frequency/wavenumber pairs (ω, k) that satisfy (2.15) define eigenmodes of the vortex sheet for given values of m, M_a, T and r_{MAX}. To find these pairs, similarly to the F-T model, we specify a frequency ω (real or complex) and compute the associated eigenvalues k. Eigenvalues are computed using a root finder based on the Levenberg–Marquardt method (Levenberg 1944; Marquardt 1963).

After imposing bounded solution for $r = 0$ and a soft-wall boundary condition at $r = r_{MAX}$, the solution for the pressure in the inner and outer flows is

$$
\left.\begin{aligned}
\hat{p}_i(r) &= B_i I_m(\gamma_i r) \quad r \leq 0.5 \\
\hat{p}_o(r) &= C_o(-z I_m(\gamma_o r) + K_m(\gamma_o r)) \quad r > 0.5,
\end{aligned}\right\}
\tag{2.17a–b}
$$

where B_i and C_o are constants fixed in order to ensure pressure continuity at the V-S location $r = 0.5$. The eigenfunctions of the other flow variables are calculated from the knowledge of $\hat{p}_{i,o}(r)$ by exploiting the Fourier-transformed LEE (A4f). The same eigenfunction normalisation procedure described for the F-T model is used for the V-S model as well.

2.3.3. *Identification of reflected and transmitted waves*

There are two types of waves which appear due to the scattering of the K–H wave at the shock: upstream-travelling reflected waves in region 1, and downstream-travelling transmitted waves in region 2 (see figure 1). Following Towne *et al.* (2017), we use the terms downstream and upstream travelling to designate the direction of the energy transfer. This property can be characterised using the Briggs–Bers criterion by looking at the asymptotic behaviour of $k(\omega)$ at large ω_i (Briggs 1964; Bers 1983). The wave is downstream travelling if

$$
\lim_{\omega_i \to +\infty} k_i = +\infty,
\tag{2.18a}
$$

and upstream travelling if

$$
\lim_{\omega_i \to +\infty} k_i = -\infty,
\tag{2.18b}
$$

where the subscript i stands for the imaginary part of the variable. The downstream- and upstream-travelling waves are denoted hereinafter with the superscript $+$ and $-$, respectively.

2.3.4. *Mean flow*

The conditions upstream of the shock in the case of the V-S are provided by

$$
r \leq 0.5 \begin{cases} \bar{u}_{1x} = M_{a_1} \\ \bar{p}_1 = \dfrac{\rho T}{\gamma} \\ \bar{\rho}_1 = \rho \\ \bar{T}_1 = \dfrac{T}{\gamma - 1} \end{cases} \qquad (2.19a) \qquad r > 0.5 \begin{cases} \bar{u}_{1x} = 0 \\ \bar{p}_1 = \dfrac{1}{\gamma} \\ \bar{\rho}_1 = 1 \\ \bar{T}_1 = \dfrac{1}{\gamma - 1}, \end{cases} \qquad (2.19b)
$$

where $\rho = \rho_j / \rho_\infty$ is the jet-to-ambient density ratio.

In the case of finite thickness, we use the hyperbolic tangent function reported in Lesshafft & Huerre (2007) for the velocity profile upstream of the shock,

$$
\bar{u}_{1x} = \frac{1}{2} M_{a_1} \left(1 + \tanh \left(\frac{R}{4\delta} \left(\frac{R}{r} - \frac{r}{R} \right) \right) \right), \qquad (2.20)
$$

where δ is the shear-layer momentum thickness and $R = 0.5$ is the nozzle radius. Consistent with particle image velocimetry results presented in Mancinelli *et al.* (2021) for an under-expanded supersonic jet with jet Mach number $M_{j_1} = 1.1$ and temperature ratio $T \approx 0.81$, we choose a shear-layer thickness $R/\delta = 10$. Denoting the dimensional variables with the superscript $*$ and the fully expanded variables with the subscript j, the mean density profile is calculated as the inverse of the mean temperature profile, $\rho^*(r)/\rho_j = (T^*(r)/T_j)^{-1}$, where the mean temperature is calculated using the Crocco–Busemann relation (Michalke 1984)

$$
\frac{T^*(r)}{T_j} = \frac{T_\infty}{T_j} + \left(1 - \frac{T_\infty}{T_j} \right) \frac{u_x^*(r)}{U_j} + (\gamma - 1) M_j^2 \frac{u_x^*(r)}{U_j} \frac{1}{2} \left(1 - \frac{u_x^*(r)}{U_j} \right). \qquad (2.21)
$$

The mean flow downstream of the shock can then be determined from the upstream conditions using the jump equations of normal shocks

$$
\left. \begin{aligned}
M_{j_2} &= \sqrt{\frac{M_{j_1}^2 (\gamma - 1) + 2}{2\gamma M_{j_1}^2 - (\gamma - 1)}}, \\
\frac{\bar{p}_2}{\bar{p}_1} &= \frac{2\gamma M_{j_1}^2 - (\gamma - 1)}{\gamma + 1}, \\
\frac{\bar{\rho}_2}{\bar{\rho}_1} &= \frac{(\gamma + 1) M_{j_1}^2}{(\gamma - 1) M_{j_1}^2 + 2}, \\
\frac{\bar{T}_2}{\bar{T}_1} &= \frac{\left(1 + \dfrac{\gamma - 1}{2} M_{j_1}^2 \right) \left(\dfrac{2\gamma}{\gamma - 1} M_{j_1}^2 - 1 \right)}{M_{j_1}^2 \left(\dfrac{2\gamma}{\gamma - 1} + \dfrac{\gamma - 1}{2} \right)}.
\end{aligned} \right\} \qquad (2.22a\text{–}d)
$$

The mean-flow profiles upstream and downstream of the shock in the case of V-S and F-T models for the flow conditions listed above are represented in figure 2. The presence of the shock wave generates a mean pressure gradient along the radial direction downstream of the shock. This $\partial \bar{p}/\partial r$ induces a mean radial velocity $\bar{u}_r$, thus making the flow slowly diverging. The evaluation of this induced radial velocity in the case of a F-T model is
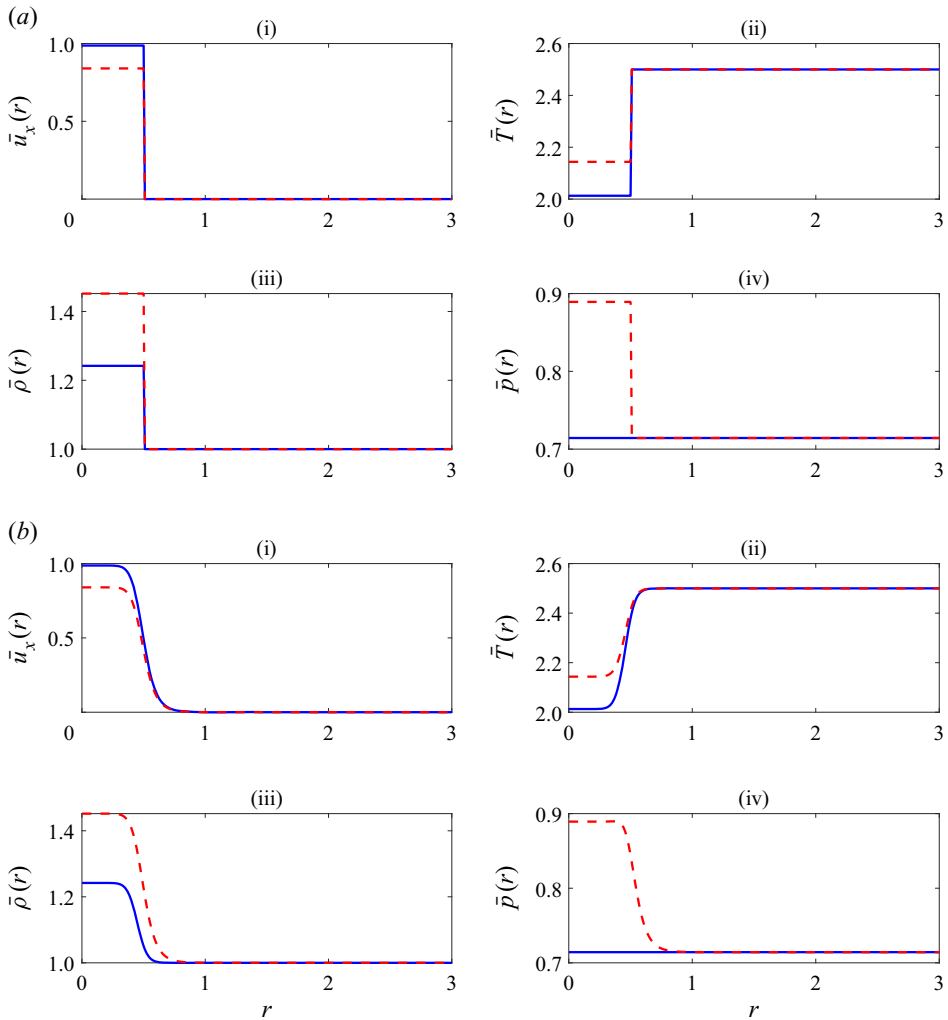
954 A9-9

Figure 2. Mean flow upstream and downstream of the shock for the V-S and F-T models for $M_{j_1} = 1.1$: solid blue lines refer to upstream conditions, dashed red lines to downstream ones. (*a*) The V-S model, (*b*) F-T model: (i) axial velocity, (ii) temperature, (iii) density, (iv) pressure.

reported in Appendix C, where we show that the induced mean radial velocity is small compared with the axial velocity component. We also point out that the transmission and reflection mechanisms occur locally and hence they are not affected by the flow evolution far away from the shock.

3. Results

In this section we present the results of the reflection-coefficient calculation obtained by modelling the jet dynamics with both the V-S and F-T models. We first consider a Strouhal number $St = 0.68$, a jet Mach number $M_{j_1} = 1.1$ and a temperature ratio $T \approx 0.81$ (corresponding to an acoustic Mach number $M_{a_1} \approx 0.987$), which results in a jet Mach number $M_{j_2} = 0.91$ and an acoustic Mach number $M_{a_2} \approx 0.84$ downstream of the shock. These upstream jet conditions and Strouhal number are selected to match conditions

954 A9-10

for which screech has been experimentally observed by Mancinelli *et al.* (2019*a*, 2021). Due to the axisymmetric nature of the resonance mode, we here study the azimuthal mode $m = 0$. Furthermore, we focus on the reflection coefficient of the upstream-travelling guided mode of the second radial order given that this mode has been proven to be the closure mechanism for axisymmetric screech modes (see Edgington-Mitchell *et al.* 2018; Mancinelli *et al.* 2019*a*, 2021). Finally, for the F-T model, we explore the variation of the reflection coefficient as a function of both St and M_j.

3.1. *Incident, reflected and transmitted waves*

First, we identify the reflected and transmitted waves generated by the interaction of the incident K–H wave with the shock discontinuity for both the V-S and F-T models upstream and downstream of the shock, respectively. Figure 3 shows the V-S eigenspectrum in the complex-k plane upstream of the shock. For the sake of brevity and clarity of the figure, in the present manuscript we show eigenvalues only for real ω (see Mancinelli *et al.* (2022) for the corresponding eigenspectrum for $\omega \in \mathcal{C}$). Several distinct families of modes can be identified. The V-S model supports one convectively unstable mode, the K–H mode, which is denoted hereinafter k_{KH}. The unstable k_{KH} wave has a complex conjugate and both eigenvalues have positive phase and group velocities according to the criteria (2.18). The V-S model also supports guided modes, i.e. modes that use the jet as a wave guide. These modes, hereinafter denoted k_p, belong to a hierarchical family of waves identified by their azimuthal and radial orders m and n_r, respectively. According to Towne *et al.* (2017), these modes are guided or completely trapped inside the jet depending on the St and the radial order considered. Specifically, we observe evanescent k_p waves for $n_r = 1$ with supersonic negative phase speed. The wave associated with $k_i > 0$ is a downstream-travelling wave, whereas the wave with $k_i < 0$ is upstream travelling. The k_p mode for $n_r = 2$ is propagative and upstream travelling and has a slightly subsonic negative phase speed. All the $k_p^{\pm}$ modes with $n_r \leq 2$ have support both inside and outside of the jet for the St analysed. The k_p^+ modes for $n_r > 2$ represent acoustic waves trapped inside the jet due to total reflection at the V-S, which effectively behaves as a soft-walled duct (Towne *et al.* 2017; Martini, Cavalieri & Jordan 2019). Finally, we find propagative and evanescent acoustic modes, which are hereinafter denoted k_a. Among them, modes lying on the real and imaginary axes with $k_r < 0$ and $k_i < 0$, respectively, are upstream-travelling modes.

Figure 4 shows the eigenspectrum upstream of the shock computed using linear stability theory for a shear layer with finite thickness $R/\delta = 10$. In addition to the mode families supported by the V-S, the F-T model supports critical-layer modes, denoted hereinafter k_{cr}. These modes have positive, subsonic phase and group velocities and lie on the real axis. Their spatial support is concentrated in the critical layer of the jet, i.e. the region of the jet where the phase speed equals the local mean-flow velocity (Tissot *et al.* 2017). Critical-layer modes with small wavenumbers are characterised by a spatial support mainly concentrated in the core of the jet and possess a phase speed close to the mean jet velocity, whereas k_{cr} modes with larger wavenumbers are mostly concentrated in the shear layer and have a phase-speed value which decreases as the spatial support of the mode moves more and more outside of the jet. To summarise, both the V-S and F-T models support two families of reflected waves upstream of the shock: (i) guided jet modes and (ii) propagative and evanescent acoustic modes. Among the guided modes, we may distinguish the evanescent k_p^- mode with $n_r = 1$ and the propagative k_p^- mode with $n_r = 2$. In the remainder of this paper, we focus our attention on the reflection coefficient between the K–H wave and the propagative k_p^- mode with $n_r = 2$, since this interaction is responsible
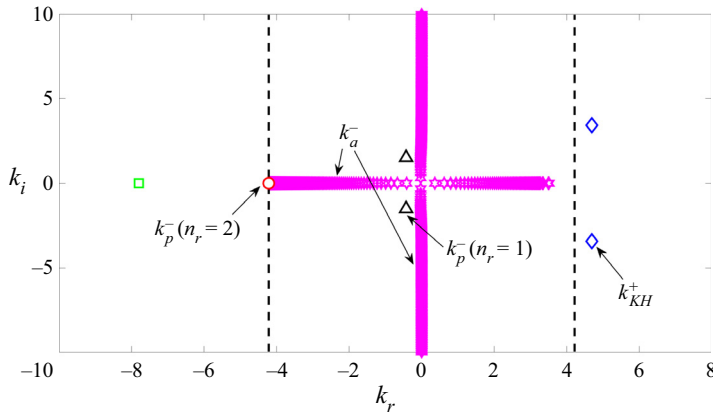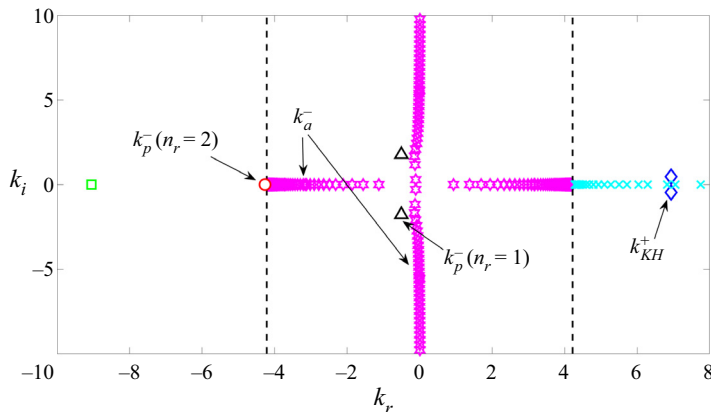
Figure 3. Eigenspectrum upstream of the shock obtained using the V-S model for azimuthal mode $m = 0$, $T \approx 0.81$, $M_{j_1} = 1.1$ and $\omega \in \mathcal{R}$. Blue $\diamond$ represent k_{KH}^+ and k_{KH}^{*+} waves, red $\circ$ represents propagative k_p^- mode with $n_r = 2$, black $\triangle$ represent evanescent $k_p^\pm$ modes with $n_r = 1$, green $\square$ represent k_p^+ modes with $n_r \geq 2$, magenta $*$ represent $k_a^\pm$ waves. Dashed lines refer to the sonic speed $\pm c_\infty$. Incident and reflected waves are indicated with arrows and labelled.

Figure 4. Eigenspectrum upstream of the shock obtained using the F-T model for azimuthal mode $m = 0$, $T \approx 0.81$, $M_{j_1} = 1.1$ and $\omega \in \mathcal{R}$. Markers and colours to identify the modes are the same used in figure 3 in the case of the V-S. The modes that are only supported by the F-T model, that is the k_{cr}^+ modes, are here indicated by cyan $\times$. Dashed lines refer to the sonic speed $\pm c_\infty$. Incident and reflected waves are indicated with arrows and labelled.

for the screech resonance at this frequency and Mach number (Edgington-Mitchell *et al.* 2018; Mancinelli *et al.* 2019a, 2021; Nogueira *et al.* 2022).

We now consider the eigenspectrum downstream of the shock with the aim of identifying the transmitted modes for both the V-S and F-T models. Figure 5 shows the eigenspectrum obtained using the V-S. According to Towne *et al.* (2017), in the subsonic regime for $0.82 \leq M < 1$ the guided modes are characterised by two upstream-travelling branches delimited by two saddle points in the k_r-*St* plane: one branch characterised by a larger negative phase speed close to the ambient speed of sound, the above-defined k_p^-, and one with a lower phase-speed absolute value, herein denoted k_d^-. Similar to the eigenspectrum upstream of the shock, we may identify the k_{KH}^+ wave and its complex
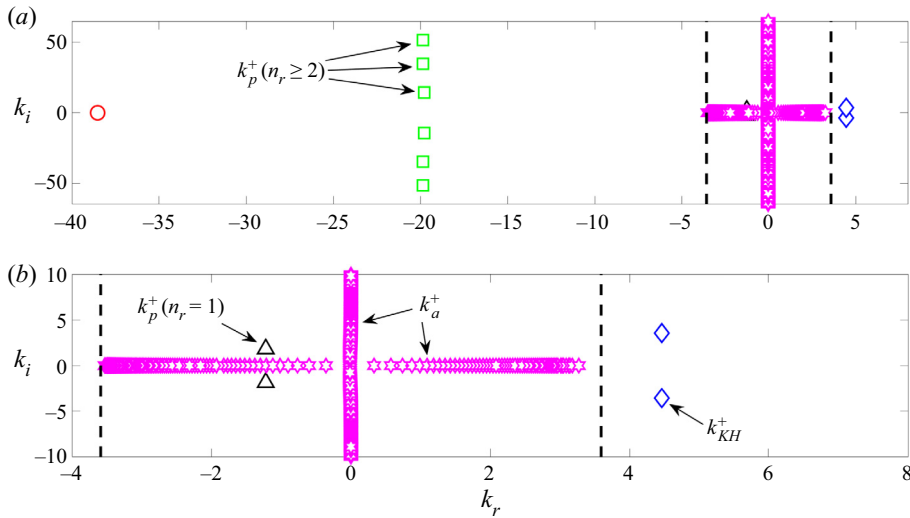
954 A9-12

Figure 5. Eigenspectrum downstream of the shock obtained using the V-S model for $\omega \in \mathcal{R}$, azimuthal mode $m = 0$, $T \approx 0.85$ and $M_{j_2} = 0.91$ (which corresponds to $M_{a_2} = 0.84$): (*a*) global view, (*b*) zoom around the origin. Blue $\diamond$ represent k_{KH}^+ and k_{KH}^{*+} waves, red $\circ$ represents propagative k_d^- mode with $n_r = 1$, black $\triangle$ represent evanescent $k_p^{\pm}$ modes with $n_r = 1$, green $\square$ represent $k_p^{\pm}$ modes with $n_r \geq 2$, magenta $*$ represent $k_a^{\pm}$ waves. Dashed lines refer to the sonic speed $\pm c_\infty$. Transmitted waves are indicated with arrows and labelled.

conjugate k_{KH}^{*+}, the downstream- and upstream-travelling k_p waves with $n_r = 1$, which are evanescent and have supersonic negative phase speed at this frequency, and the $k_a^{\pm}$ modes. As outlined in Mancinelli *et al.* (2022), propagative, downstream-travelling acoustic modes are not found in the vicinity of the sonic line due to numerical issues in the root-finder algorithm. We show in Appendix D that these modes are not relevant for the determination of the reflection coefficient. We then locate the upstream-travelling propagative k_d^- wave for $n_r = 1$, which has a duct-like behaviour (Towne *et al.* 2017), and the evanescent $k_p^{\pm}$ waves with $n_r \geq 2$, which behave like modes in a soft duct as well at this frequency. In this regard, we note that the k_p eigenvalues with $k_i > 0$ are associated with k^+ waves, whereas the eigenvalues with $k_i < 0$ are associated with k^- modes.

Figure 6 shows the eigenspectrum downstream of the shock computed using a F-T model. Unlike those computed by the V-S, the evanescent guided modes for $n_r > 1$ bend towards the supersonic phase-speed region as n_r increases and eventually merge with the evanescent free-stream acoustic modes for $n_r > 4$. Additionally, we observe the k_{cr}^+ waves that are not supported by the V-S. To summarise, within the V-S model, possible downstream-travelling transmitted modes are: (i) the K–H mode and its complex conjugate, (ii) the evanescent guided mode of first radial order with supersonic phase speed, (iii) the evanescent trapped modes of higher radial order with subsonic phase speed and (iv) the acoustic modes. For the F-T model, in addition to the transmitted modes listed above for the V-S, we include the critical-layer modes. For this flow model, unlike the V-S model and consistent with the eigenspectrum shown in figure 6, we use evanescent k_p^+ waves on the transmitted side up to the radial order $n_r = 4$, that is, before this mode branch merges with the evanescent k_a^+ modes and become no longer distinguishable. A summary of the modes involved in the reflection coefficient computation is reported in table 1.

Examples of the normalised pressure eigenfunctions of the waves upstream and downstream of the shock are reported in figure 7. For the V-S (figure 7*a*), the incident and
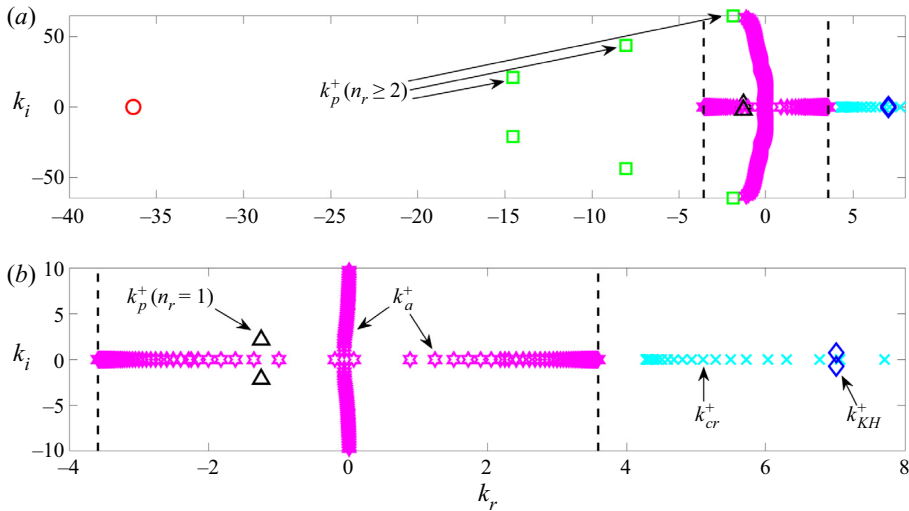
Figure 6. Eigenspectrum downstream of the shock obtained using the F-T model for $\omega \in \mathcal{R}$, azimuthal mode $m = 0$, $T \approx 0.85$ and $M_{j_2} = 0.91$ (which corresponds to $M_{a_2} = 0.84$): (*a*) global view, (*b*) zoom around the origin. Markers and colours are the same as used in figure 5 to identify the modes in the case of the V-S. The modes that are only supported by the F-T model, that is the k_{cr}^+ modes, are here indicated by cyan ×. Dashed lines refer to the sonic speed $\pm c_\infty$. Transmitted waves are indicated with arrows and labelled.

	Vortex sheet	Finite thickness
Incident	k_{KH}^+	k_{KH}^+
Reflected	propagative k_p^- with $n_r = 2$ evanescent k_p^- with $n_r = 1$ propagative and evanescent k_a^-	propagative k_p^- with $n_r = 2$ evanescent k_p^- with $n_r = 1$ propagative and evanescent k_a^-
Transmitted	k_{KH}^+ and k_{KH}^{*+} evanescent k_p^+ with $n_r \geq 1$ propagative and evanescent k_a^+ —	k_{KH}^+ and k_{KH}^{*+} evanescent k_p^+ with $n_r \geq 1$ propagative and evanescent k_a^+ k_{cr}^+

Table 1. Summary of the eigenmodes supported by the V-S and F-T models involved in the reflection coefficient computation.

transmitted K–H waves show a peak at the V-S location and the reflected waves, that is k_p^- and k_a^- modes, have support both inside and outside the jet. We note that, although there is no energy loss at $r = r_{MAX}$ as a consequence of the imposition of a soft-wall boundary condition, the energy of k_a modes reflected back cannot be transferred to the other discrete modes since the flow is locally parallel. On the transmitted side downstream of the shock, while the evanescent k_p^+ wave with $n_r = 1$ has a support both in the inner and outer part of the jet, the transmitted k_p^+ modes with $n_r > 1$ show a spatial support concentrated inside the jet, consistent with their identity as acoustic waves trapped within the jet core. Examples of the pressure eigenfunctions of the waves upstream and downstream of the shock computed using the F-T model are shown in figure 7(*b*). The incident K–H mode and the reflected k_p^- and k_a^- have a similar shape to that found using the V-S model.
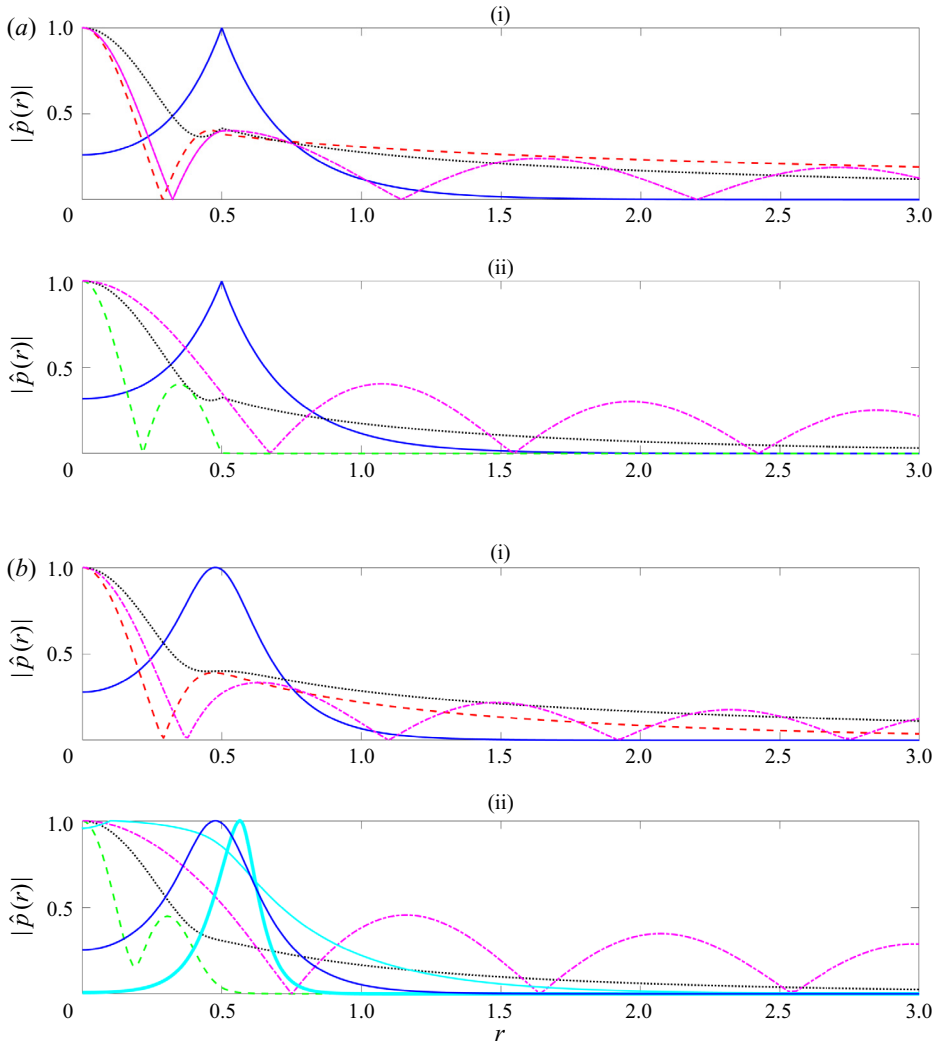
954 A9-14

Figure 7. Pressure eigenfunctions for $m = 0$ and $St = 0.68$ computed using (*a*) the V-S model and (*b*) the F-T model. The colours are the same as those used in figures 3, 4, 5 and 6 to identify the different mode families upstream and downstream of the shock, respectively. (i) Incident and reflected waves upstream of the shock for $M_j = 1.1$ and $T \approx 0.81$: solid blue line refers to the incident k_{KH}^+ wave, dashed red line to the propagative k_p^- wave with $n_r = 2$, dotted black line to the evanescent k_p^- mode with $n_r = 1$, dash-dotted magenta line to the propagative k_a^- wave. (ii) Transmitted waves downstream of the shock for $M_{j_2} = 0.91$ and $T \approx 0.85$: solid blue line refers to the transmitted k_{KH}^+ mode, dotted black line to the evanescent k_p^+ with $n_r = 1$, dashed green line to the evanescent k_p^+ with $n_r = 2$, dash-dotted magenta line to the propagative k_a^+ wave, solid and bold cyan lines to k_{cr}^+ modes.

As mentioned above, k_{cr}^+ modes have eigenfunctions with a spatial support concentrated either inside of the jet or in the shear layer depending on the wavenumber value considered. The spatial support of the critical-layer modes moves to larger r and the phase velocity U_ϕ decreases as $|k_{cr}|$ increases.
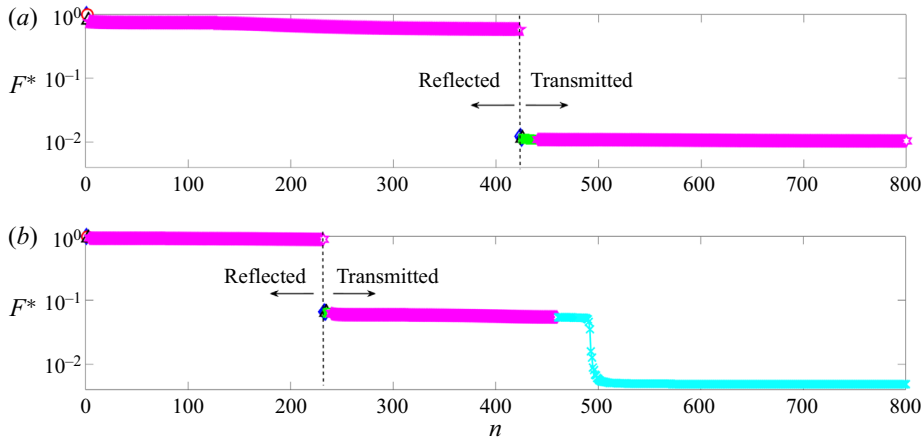
Figure 8. Evolution of the normalised objective function as a function of the number of modes: (*a*) V-S, (*b*) F-T model. Markers and colours are the same as those used to identify the modes in the eigenspectra in figures 3 and 5 for the V-S and figures 4 and 6 for the F-T model.

3.2. *Reflection coefficient*

Second, we present the reflection-coefficient values calculated by minimising the error objective function F in (2.8) via the pseudo-inverse solution (2.12). Figure 8 shows the evolution of the objective function F as a function of the number of reflected and transmitted modes $n = n_R + n_T$ for both the V-S and F-T models. Here, F is normalised so as to have unitary value when the sole incident K–H wave is considered in the minimisation algorithm, thus allowing us to quantify the relevance of the modes added in the computation in terms of error reduction. We here make a convergence analysis showing how the objective function changes by adding reflected and transmitted modes. In the absence of any unquestionable criterion allowing us to know *a priori* the relevance of each mode in the reflection/transmission dynamics, we choose to add modes as a function of the family they belong to. For each mode family, waves are added by increasing $|k|$. Specifically, we first add in the calculation the reflected waves, that is the k_p^- and k_a^- mode families, and then we add the transmitted modes downstream of the shock, that is k_{KH}^+ and its complex conjugate, the k_p^+ modes for $n_r \geq 1$, the k_a^+ modes and the k_{cr}^+ waves in the case of the F-T model, for a total number of modes $N = N_R + N_T = 800$. The final results are independent of the mode arrangement. The objective function remains approximately constant when reflected waves are added. The transmitted K–H mode provides a significant decay in the cost function, which indicates that it has an important role in the reflection/transmission mechanism, as the impinging and transmitted K–H modes have a similar structure. For the V-S, the addition of the other transmitted modes has a small impact on the cost functional, which saturates at a value of $\approx 10^{-2}$. On the contrary, for the F-T model, the addition of critical-layer modes produces an important reduction of the cost function, which saturates at a value of 5×10^{-3}, lower than that observed in the case of the V-S.

Figure 9 shows the evolution of the amplitude and phase of the reflection coefficient associated with the upstream-travelling guided mode of second radial order as a function of the number of modes n obtained using the V-S model. On the reflected side, the significant drop of $|R|$ observed when k_a^- modes are added is due to propagative acoustic modes.
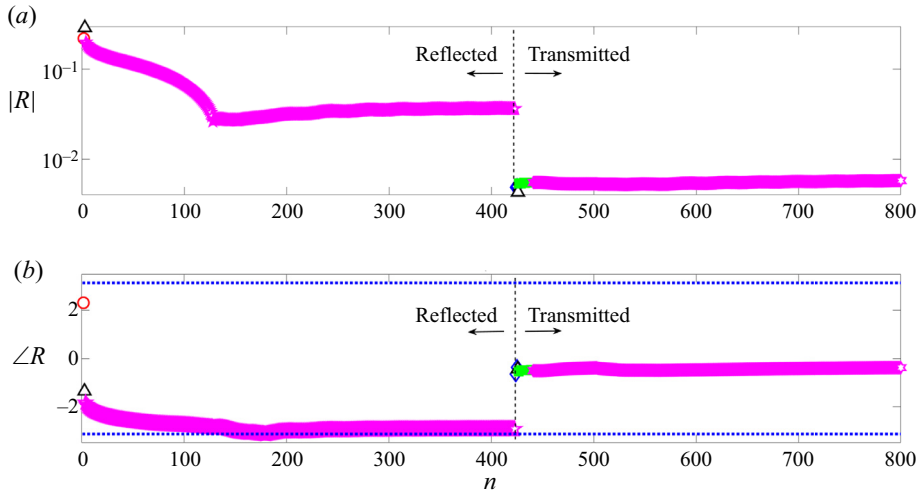
Figure 9. Evolution of the reflection coefficient computed using the V-S as a function of the modes considered in the calculation (markers and colours are the same as those used to identify the modes in the eigenspectra in figures 3 and 5): (*a*) amplitude, (*b*) phase. Blue dotted lines indicate $\pm\pi$ in the phase plot.

Similar to the objective function in figure 8(*a*), both the amplitude and phase of the reflection coefficient undergo a significant jump when modes on the transmitted side are included in the calculation. Specifically, the solution does not drastically change after the inclusion of the k_{KH}^{+} mode and remains approximately constant. The solution converges to 5.8×10^{-3} and -0.38 for the amplitude and phase, respectively.

The evolution of the amplitude and phase of the reflection coefficient as a function of n in the case of the F-T model is shown in figure 10. Similar to the V-S model, we see a significant change in the value of both amplitude and phase when modes on the transmitted side are included in the calculation. Consistent with what we observed in the objective function trend, the addition of the k_{cr}^{+} modes plays an important role in the determination of the reflection coefficient. Specifically, a significant drop in amplitude occurs for critical-layer modes with $5.5 \leq |k| \leq 21$, after which both the amplitude and phase values remain approximately constant. These are modes with wavelength in the range $\approx [0.3D, D]$ and, hence, 6 to 20 times the shear-layer thickness. Their phase speed is $\approx 0.2U_j \leq U_\phi \leq 0.75U_j$, and they are mostly concentrated in the centre of the shear layer, as shown in figure 11.

A summary of the reflection-coefficient values obtained for both flow models is reported in table 2. A large discrepancy between the V-S and F-T model is found for both the amplitude and phase of the reflection coefficient. This result suggests that the presence of a finite thickness and the associated shear-layer dynamics, which cannot be described using a vortex sheet, plays an important role in the reflection/transmission mechanism and needs to be taken into account to perform a reliable estimation of the reflection coefficient.

3.2.1. *Reflected and transmitted pressure fields*

The reflected and transmitted pressure fields for the flow condition investigated above using a F-T model are here reconstructed in the *x–r* plane. Using the normal-mode ansatz
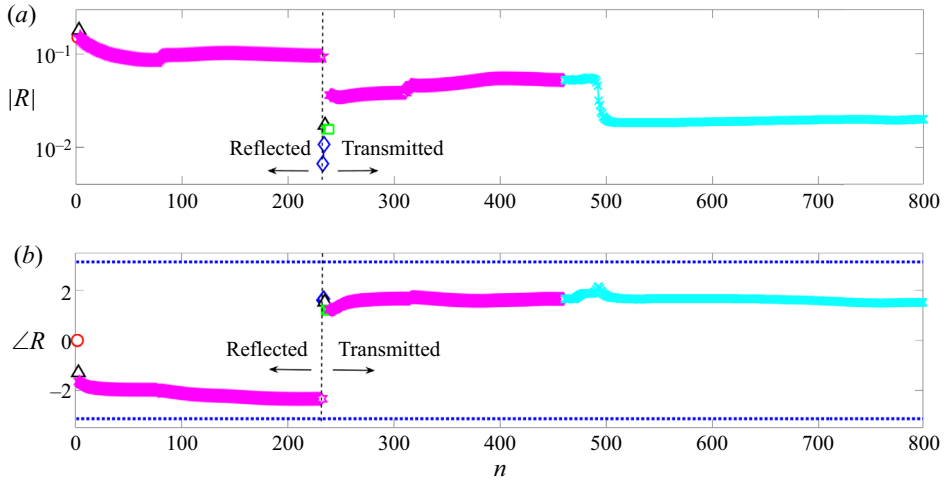
Figure 10. Evolution of the amplitude and phase of the reflection coefficient computed using the F-T model as a function of the number of modes considered. Markers and colours are the same as those used in figures 4 and 6 to identify the mode families. (*a*) amplitude, (*b*) phase. Blue dotted lines indicate $\pm\pi$ in the phase plot.
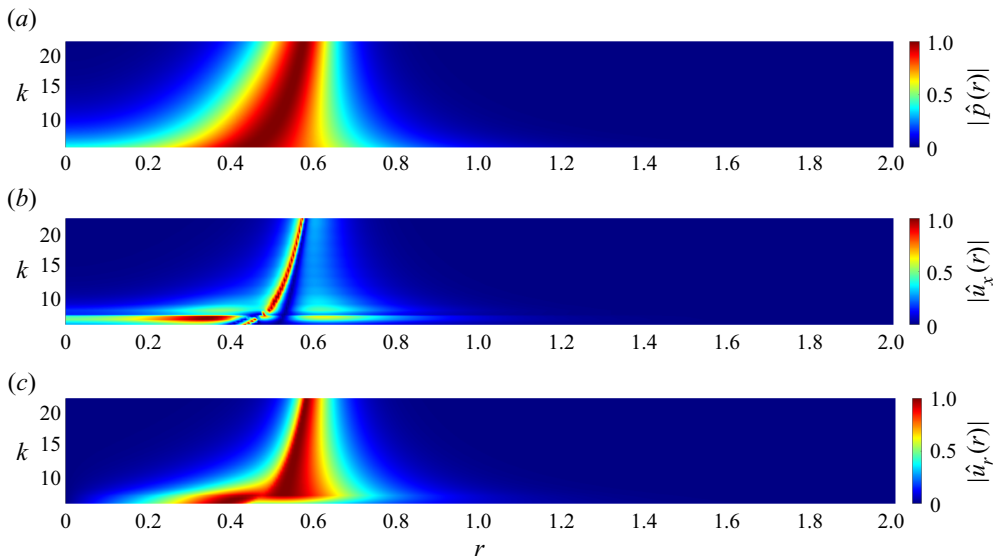

Figure 11. Normalised eigenfunctions of k_{cr}^{+} modes computed using the F-T model as a function of wavenumber k and radial distance r: (*a*) pressure, (*b*) axial velocity, (*c*) radial velocity.

	Reflection-coefficient values	
	Amplitude	Phase
Vortex sheet (V-S)	0.0058	−0.38
Finite thickness (F-T)	0.02	1.5

Table 2. Summary of the reflection-coefficient values associated with the upstream-travelling guided mode of second radial order generated by the interaction between an incident K–H wave on a shock. Results obtained using both the V-S and F-T models to describe the jet dynamics are reported.
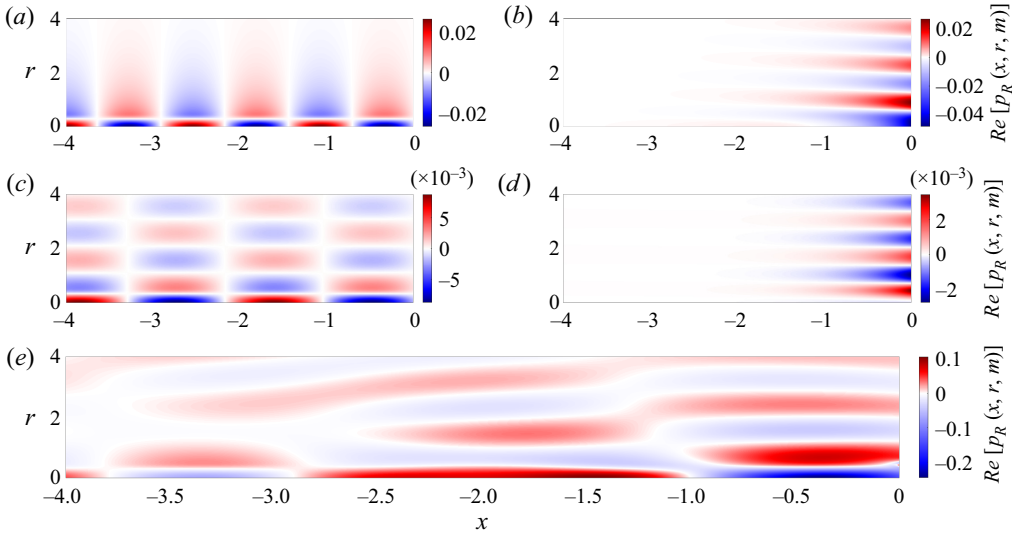
Figure 12. Reconstruction of the reflected fields in the $x - r$ plane for a shock discontinuity located at $x = 0$: (a) k_p^- mode with $n_r = 2$, (b) k_p^- mode with $n_r = 1$, (c) propagative k_a^- wave, (d) evanescent k_a^- wave, (e) total field.

(2.4), the reflected and transmitted fields are given by

$$p_R(x, r, \theta) = \sum_{n_R=1}^{N_R} R_{n_R} \hat{p}_{1R, n_R} \exp(i (k_{nR}x + m\theta)), \tag{3.1a}$$

$$p_T(x, r, \theta) = \sum_{n_T=1}^{N_T} T_{n_T} \hat{p}_{2T, n_T} \exp(i (k_{nT}x + m\theta)). \tag{3.1b}$$

We set $x = 0$ to be the location of the shock discontinuity, so the reflected upstream-travelling and transmitted downstream-travelling waves evolve along negative and positive x directions, respectively. Figure 12 shows the entire reflected field as well as the reflected fields for each type of the upstream-travelling modes considered in the reflection-coefficient calculation, that is the propagative k_p^- mode with $n_r = 2$, the evanescent k_p^- mode with $n_r = 1$ and an example of the propagative and evanescent k_a^- waves with $|k| \approx 2.79$ and 2.1, respectively. The fields reconstructed using the k_p^- modes show a spatial support both inside and outside the jet with a prescribed radial decay. Regarding the axial evolution, the evanescent k_p^- mode with $n_r = 1$ exhibits a decay starting from the shock position $x = 0$, whereas the k_p^- mode with $n_r = 2$ has a fixed axial structure consistent with its neutrally stable nature. A similar behaviour is found for the pressure fields reconstructed using propagative and evanescent free-stream acoustic waves. The entire reflected pressure field, which results from the linear superposition of all the reflected k^- waves, shows an axially and radially decaying structure starting from $x = 0$ and $r = 0$, respectively.

The entire transmitted field as well as the transmitted fields for each mode family considered in the reflection-coefficient calculation are shown in figure 13. We here report the fields obtained using the k_{KH}^+ wave, the evanescent supersonic k_p^+ mode with $n_r = 1$, the evanescent subsonic k_p^+ mode with $n_r = 2$, the propagative and evanescent k_a^+ waves
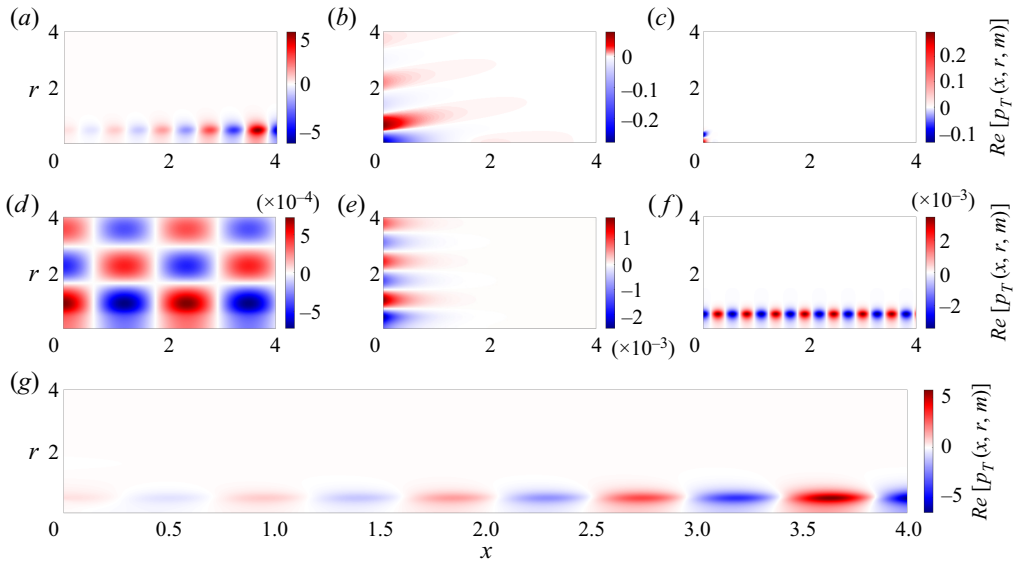
Figure 13. Reconstruction of the transmitted fields in the x–r plane for a shock discontinuity located at $x = 0$: (a) k_{KH}^+ wave, (b) supersonic k_p^- mode with $n_r = 1$, (c) subsonic k_p^+ with $n_r = 2$, (d) propagative k_a^+ wave, (e) evanescent k_a^+ wave, (f) k_{cr}^+ mode, (g) total field.

with $|k| \approx 2.7$ and 2.8, respectively, and the k_{cr}^+ mode for $|k| \approx 11.5$. Consistent with its unstable nature, the shape and intensity of the total transmitted field is dominated by the K–H mode. The shape of the transmitted fields reconstructed using the individual mode family is consistent with the neutral/evanescent nature and radial structure described above.

3.2.2. *Frequency–Mach-number dependence of the reflection coefficient*

We here explore the frequency–Mach-number dependence of the reflection coefficient associated with the upstream-travelling guided mode with $n_r = 2$ obtained using the F-T model. For this purpose, we let the jet Mach number vary in the range $M_j = [1, 1.7]$ and explore the Strouhal-number band for which the guided mode is propagative for such flow conditions, that is the St-number range delimited by the branch and saddle points (see Mancinelli *et al.* 2019a, 2021). The resolutions for ΔM_j and ΔSt were set equal to 10^{-2} and 5×10^{-3}, respectively. Figure 14 shows the evolution of the normalised objective function F as a function of M_j and St. The errors are very small for low M_j and gradually rise as the jet Mach number increases but never exceed 13 %. The amplitude and the phase modulus of the reflection coefficient as a function of St and M_j are shown in figure 15. The reflection-coefficient amplitude rises with increasing M_j for a given St and appears to be larger in the proximity of the saddle point for all M_j, with the jet-flow region $M_j = [1.17, 1.37]$ showing the highest amplitude. Overall, the phase gradually increases for larger M_j and lower St. We note that a jump from in-phase to out-of-phase conditions is found for $M_j = 1.58$ for most frequencies.

4. Conclusions

The scattering of a K–H wave into a discrete, upstream-travelling guided mode due to a normal shock in a jet flow was computed in the present manuscript. Jets with
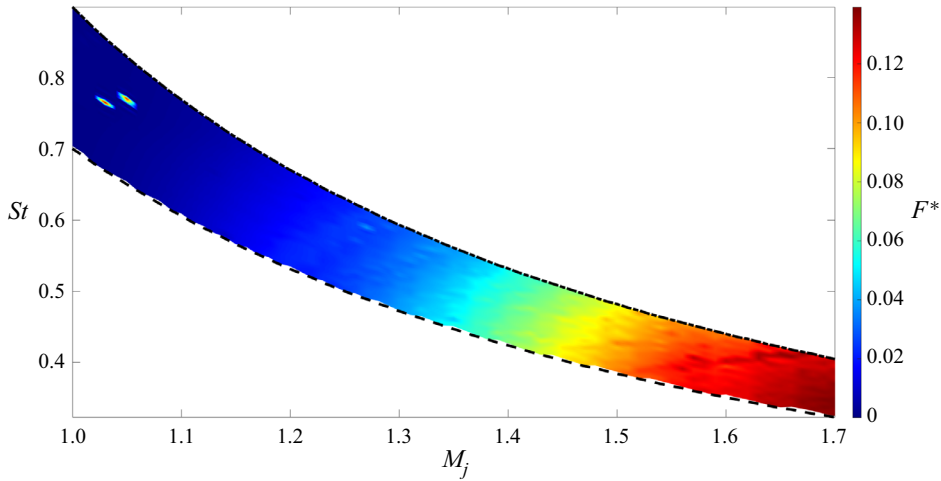
954 A9-20

Figure 14. Normalised error objective function as a function of Strouhal and jet Mach numbers for the F-T model. Dashed and dash-dotted lines refer to the branch- and saddle-point locations, respectively.
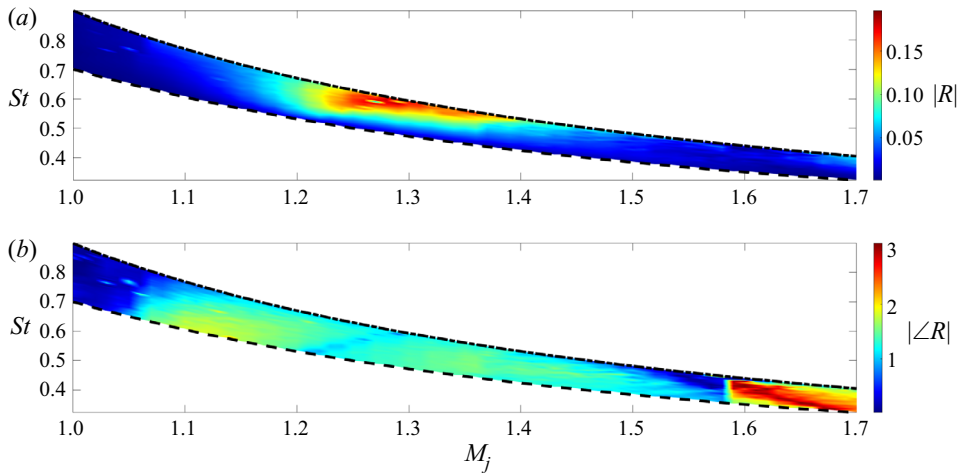

Figure 15. Evolution of the reflection coefficient as a function of Strouhal and jet Mach numbers for the F-T model. Dashed and dash-dotted lines refer to the branch- and saddle-point locations, respectively. (*a*) Amplitude, (*b*) phase.

zero-thickness and F-T shear layers were modelled with an analytical V-S and a numerical solution of the Rayleigh equation, respectively. The reflection coefficient associated with the scattered, upstream-travelling wave was calculated via a mode-matching technique enforcing conservation equations through the shock discontinuity. Assuming small disturbances, the shock equations were linearised about the mean flow and the possible scattered modes, i.e. upstream-travelling reflected waves and downstream-travelling transmitted waves, were identified by assessing the corresponding group velocity using the Briggs–Bers criteria. Solutions based on a truncated set of modes were obtained via the minimisation of the error in the conservation equations, which corresponds to a weighted pseudo-inverse solution. The F-T model showed that critical-layer modes, characterised by eigenfunctions with radial support mostly concentrated in the centre of the shear layer, by a

wavelength 6 to 20 times the shear-layer thickness and by a phase velocity between 0.2 and 0.75 of the jet velocity, play an important role in the reflection-coefficient calculation and, thus, most likely in the physical mechanisms underpinning the process. The reconstructed reflected and transmitted pressure fields in the *x–r* plane showed an organised structure consistent with the axial and radial evolution of the modes calculated by the F-T model. The frequency–Mach-number dependence of the reflection coefficient has been explored, revealing that the reflection-coefficient amplitude is larger for frequencies in the proximity of the saddle point and for jet Mach-number values in between 1.17 and 1.37. The phase exhibited a gradual increase as the Strouhal and jet Mach numbers decreased and increased, respectively.

The mode-matching approach described in this paper appears to be a relevant and promising tool for better describing and predicting resonant dynamics found in jets, such as screech in supersonic jets. A similar approach may be developed to evaluate the reflection coefficient at the nozzle exit, thus providing all the elements to make screech-frequency predictions without any input from data using the model presented in Mancinelli *et al.* (2021).

Author ORCIDs.

- Matteo Mancinelli https://orcid.org/0000-0002-7332-4335;
- Eduardo Martini https://orcid.org/0000-0002-3144-5702;
- Vincent Jaunet https://orcid.org/0000-0002-6272-1431;
- Peter Jordan https://orcid.org/0000-0001-8576-5587;
- Aaron Towne https://orcid.org/0000-0002-7315-5375.

Appendix A. Linearised Euler equations

The non-dimensional Euler equations in cylindrical coordinates are

$$
\left.
\begin{aligned}
&\frac{\mathrm{D}\rho}{\mathrm{D}t} + \rho\nabla\cdot\boldsymbol{u} = 0, \\
&\rho\frac{\mathrm{D}u_x}{\mathrm{D}t} = -\frac{\partial p}{\partial x}, \\
&\rho\left(\frac{\mathrm{D}u_r}{\mathrm{D}t} - \frac{u_\theta^2}{r}\right) = -\frac{\partial p}{\partial r}, \\
&\rho\left(\frac{\mathrm{D}u_\theta}{\mathrm{D}t} + \frac{u_r u_\theta}{r}\right) = -\frac{1}{r}\frac{\partial p}{\partial\theta}, \\
&\frac{\mathrm{D}T}{\mathrm{D}t} + (\gamma-1)\,T\nabla\cdot\boldsymbol{u} = 0, \\
&p = \frac{\gamma-1}{\gamma}\rho T,
\end{aligned}
\right\}
\tag{A1a–f}
$$

where

$$\frac{D}{Dt} = \frac{\partial}{\partial t} + u_x \frac{\partial}{\partial x} + u_r \frac{\partial}{\partial r} + \frac{u_\theta}{r} \frac{\partial}{\partial \theta}, \tag{A2a}$$

$$\nabla \cdot \boldsymbol{u} = \frac{\partial u_x}{\partial x} + \frac{\partial u_r}{\partial r} + \frac{u_r}{r} + \frac{1}{r} \frac{\partial u_\theta}{\partial \theta}. \tag{A2b}$$

Inserting the Reynolds decomposition (2.2), removing the mean and linearising, the LEE are written

$$\left.\begin{aligned}
&\frac{\partial \rho}{\partial t} + \bar{u}_x \frac{\partial \rho}{\partial x} + u_r \frac{\partial \bar{\rho}}{\partial r} + \bar{\rho} \left(\frac{\partial u_x}{\partial x} + \frac{\partial u_r}{\partial r} + \frac{u_r}{r} + \frac{1}{r} \frac{\partial u_\theta}{\partial \theta} \right) = 0, \\
&\bar{\rho} \left(\frac{\partial u_x}{\partial t} + \bar{u}_x \frac{\partial u_x}{\partial x} + u_r \frac{\partial \bar{u}_x}{\partial r} \right) = -\frac{\partial p}{\partial x}, \\
&\bar{\rho} \left(\frac{\partial u_r}{\partial t} + \bar{u}_x \frac{\partial u_r}{\partial x} \right) = -\frac{\partial p}{\partial r}, \\
&\bar{\rho} \left(\frac{\partial u_\theta}{\partial t} + \bar{u}_x \frac{\partial u_\theta}{\partial x} \right) = -\frac{1}{r} \frac{\partial p}{\partial \theta}, \\
&\frac{\partial T}{\partial t} + \bar{u}_x \frac{\partial T}{\partial x} + u_r \frac{\partial \bar{T}}{\partial r} + (\gamma - 1) \bar{T} \left(\frac{\partial u_x}{\partial x} + \frac{\partial u_r}{\partial r} + \frac{u_r}{r} + \frac{1}{r} \frac{\partial u_\theta}{\partial \theta} \right) = 0, \\
&p = \frac{\gamma - 1}{\gamma} \left(\bar{\rho} T + \bar{T} \rho \right),
\end{aligned}\right\} \tag{A3a–f}$$

where we removed the primes from the fluctuating variables for notational simplicity. The locally parallel-flow assumption implies that the derivatives along the axial and azimuthal directions x and θ are zero as well as the mean radial and azimuthal velocities $\bar{u}_r$ and $\bar{u}_\theta$. Assuming the normal-mode ansatz (2.4) yields

$$\left.\begin{aligned}
&-\mathrm{i}\omega\hat{\rho} + \bar{u}_x \mathrm{i}k\hat{\rho} + \frac{\partial \bar{\rho}}{\partial r} \hat{u}_r + \bar{\rho} \left(\mathrm{i}k\hat{u}_x + \frac{\partial \hat{u}_r}{\partial r} + \frac{\hat{u}_r}{r} + \frac{\mathrm{i}m}{r} \widehat{u_\theta} \right) = 0, \\
&\bar{\rho} \left(-\mathrm{i}\omega\hat{u}_x + \bar{u}_x \mathrm{i}k\hat{u}_x + \frac{\partial \bar{u}_x}{\partial r} \hat{u}_r \right) = -\mathrm{i}k\hat{p}, \\
&\bar{\rho} \left(-\mathrm{i}\omega\hat{u}_r + \bar{u}_x \mathrm{i}k\hat{u}_r \right) = -\frac{\partial \hat{p}}{\partial r}, \\
&\bar{\rho} \left(-\mathrm{i}\omega\hat{u}_\theta + \bar{u}_x \mathrm{i}k\hat{u}_\theta \right) = -\frac{\mathrm{i}m}{r} \hat{p}, \\
&-\mathrm{i}\omega\hat{T} + \bar{u}_x \mathrm{i}k\hat{T} + \frac{\partial \bar{T}}{\partial r} \hat{u}_r + (\gamma - 1) \bar{T} \left(\mathrm{i}k\hat{u}_x + \frac{\partial \hat{u}_r}{\partial r} + \frac{\hat{u}_r}{r} + \frac{\mathrm{i}m}{r} \widehat{u_\theta} \right) = 0, \\
&\hat{p} = \frac{\gamma - 1}{\gamma} \left(\bar{\rho}\hat{T} + \bar{T}\hat{\rho} \right).
\end{aligned}\right\} \tag{A4a–f}$$

The Fourier-transformed LEE (A4f) can be written exclusively in terms of pressure, leading to the compressible Rayleigh equation (2.13). The eigenfunctions $\hat{u}_i(r)$, $\hat{\rho}(r)$ and

$\hat{T}(r)$ are recovered from the pressure

$$\hat{u}_x(r) = -\frac{1}{\bar{\rho}(\bar{u}_x k - \omega)^2}\frac{\partial \bar{u}_x}{\partial r}\frac{\partial \hat{p}}{\partial r} - \frac{k}{\bar{\rho}(\bar{u}_x k - \omega)}\hat{p}, \tag{A5a}$$

$$\hat{u}_r(r) = -\frac{1}{\bar{\rho}(\bar{u}_x \mathrm{i}k - \mathrm{i}\omega)}\frac{\partial \hat{p}}{\partial r}, \tag{A5b}$$

$$\hat{u}_\theta(r) = -\frac{m}{\bar{\rho}r(\bar{u}_x k - \omega)}\hat{p}, \tag{A5c}$$

$$\hat{\rho}(r) = -\frac{1}{(\bar{u}_x k - \omega)^2}\left(\frac{\partial^2 \hat{p}}{\partial r^2} + \left(\frac{1}{r} - \frac{2k}{\bar{u}_x k - \omega}\frac{\partial \bar{u}_x}{\partial r}\right)\frac{\partial \hat{p}}{\partial r} - \left(k^2 + \frac{m^2}{r^2}\right)\hat{p}\right), \tag{A5d}$$

$$\hat{T}(r) = -\frac{(\gamma - 1)\bar{T}}{\bar{\rho}(\bar{u}_x k - \omega)^2}\left(\frac{\partial^2 \hat{p}}{\partial r^2} + \left(\frac{1}{r} - \frac{2k}{\bar{u}_x k - \omega}\frac{\partial \bar{u}_x}{\partial r} - \frac{1}{\bar{\rho}}\frac{\partial \bar{\rho}}{\partial r} + \frac{1}{(\gamma - 1)\bar{T}}\frac{\partial \bar{T}}{\partial r}\right)\frac{\partial \hat{p}}{\partial r}\right.$$
$$\left. - \left(k^2 + \frac{m^2}{r^2}\right)\hat{p}\right). \tag{A5e}$$

Appendix B. Energy norm derivation

Eigenfunctions are normalised to have zero phase for the pressure eigenfunction on the centreline and to have unitary energy norm. Following Chu (1965), the energy norm is defined as

$$E = \frac{1}{2}\int_V \left(A u_i^* u_i + B \rho^* \rho + C T^* T\right)\mathrm{d}V, \tag{B1}$$

where the $*$ indicates the complex conjugate and the constants A, B and C have to determined on the basis of the flow considered (Hanifi *et al.* 1996). We assume a medium at rest, thus implying $\bar{u}_x = 0$ and $\partial \bar{q}/\partial r = 0$. Hence, the LEE reduce to the following:

$$\left.\begin{aligned}
&\frac{\partial \rho}{\partial t} + \bar{\rho}\nabla \cdot \boldsymbol{u} = 0, \\
&\bar{\rho}\frac{\partial u_x}{\partial t} = -\frac{\partial p}{\partial x}, \\
&\bar{\rho}\frac{\partial u_r}{\partial t} = -\frac{\partial p}{\partial r}, \\
&\bar{\rho}\frac{\partial u_\theta}{\partial t} = -\frac{1}{r}\frac{\partial p}{\partial \theta}, \\
&\frac{\partial T}{\partial t} + (\gamma - 1)\bar{T}\nabla \cdot \boldsymbol{u} = 0, \\
&p = \frac{\gamma - 1}{\gamma}\left(\bar{\rho}T + \bar{T}\rho\right),
\end{aligned}\right\} \tag{B2a–f}$$

where we have removed the prime for the fluctuating part for notational simplicity. We calculate the time evolution of the energy norm

$$\frac{\partial E}{\partial t} = \frac{\partial E}{\partial u_i}\frac{\partial u_i}{\partial t} + \frac{\partial E}{\partial \rho}\frac{\partial \rho}{\partial t} + \frac{\partial E}{\partial T}\frac{\partial T}{\partial t}, \tag{B3}$$

which, exploiting (B2*a*), can be written as

$$\frac{\partial E}{\partial t} = -\frac{1}{2} \int_V \left(A u_i \frac{1}{\bar{\rho}} \nabla p + B \rho \bar{\rho} \nabla \cdot \boldsymbol{u} + CT (\gamma - 1) \bar{T} \nabla \cdot \boldsymbol{u} \right) dV. \tag{B4}$$

Expressing $\rho = (\gamma / \gamma - 1)(p/\bar{T}) - (\bar{\rho}/\bar{T})T$ from (B2*f*) and applying integration by parts on the first term on the right-hand side of (B4), the time evolution of the energy norm becomes

$$\frac{\partial E}{\partial t} = -\int_{\partial V} u_i p \, dS + \int_V \left(\frac{A}{\bar{\rho}} p - B \bar{\rho} \left(\frac{\gamma}{\gamma - 1} \frac{p}{\bar{T}} - \frac{\bar{\rho}}{\bar{T}} T \right) - CT (\gamma - 1) \bar{T} \right) \nabla \cdot \boldsymbol{u} \, dV, \tag{B5}$$

where $\int_{\partial V} u_i p \, dS$ represents the acoustic power crossing the domain V. Hence, $\partial E / \partial t + \int_{\partial V} u_i p \, dS$ can be interpreted as the total energy variation, which we impose to be conservative thus leading to the following expression:

$$\int_V \left(\frac{A}{\bar{\rho}} - B \frac{\bar{\rho}}{\bar{T}} \frac{\gamma}{\gamma - 1} \right) p \nabla \cdot \boldsymbol{u} \, dV + \int_V \left(B \frac{\bar{\rho}^2}{\bar{T}} - C (\gamma - 1) \bar{T} \right) T \nabla \cdot \boldsymbol{u} \, dV = 0. \tag{B6}$$

Equation (B6) can be equal to zero if and only if

$$\left. \begin{aligned} \frac{A}{\bar{\rho}} - B \frac{\bar{\rho}}{\bar{T}} \frac{\gamma}{\gamma - 1} &= 0, \\ B \frac{\bar{\rho}^2}{\bar{T}} - C (\gamma - 1) \bar{T} &= 0. \end{aligned} \right\} \tag{B7a–b}$$

By legitimately imposing $A = \bar{\rho}$, it is straightforward to calculate the values for the other two constants

$$\left. \begin{aligned} B &= \frac{\gamma - 1}{\gamma} \frac{\bar{T}}{\bar{\rho}}, \\ C &= \frac{\bar{\rho}}{\gamma \bar{T}}. \end{aligned} \right\} \tag{B8a–b}$$

For an inviscid locally parallel flow with medium at rest, the energy norm is finally given by (2.14).

Appendix C. Mean radial velocity downstream of the shock

The presence of the shock wave generates a mean pressure gradient along the radial direction downstream of the shock. This induces the appearance of a mean radial velocity. This radial velocity is here evaluated in the case of a finite thickness model in order to establish that it does not affect the calculation of the reflection coefficient. We consider the momentum equation along the radial direction (A1*c*). The conservation equation for
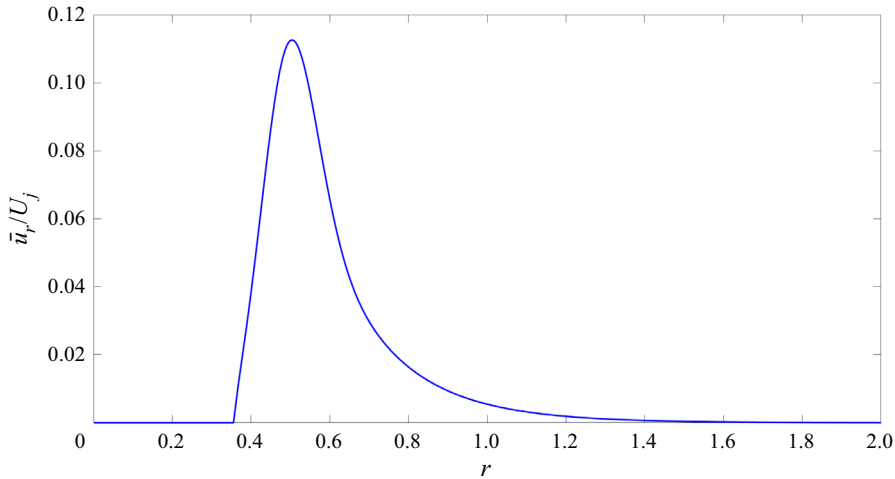
Figure 16. Mean radial velocity profile along the radial direction downstream of the shock for M_{j_1} and M_{j_2} equal to 1.1 and 0.91, respectively.

the mean flow is

$$\bar{\rho}\bar{u}_r \frac{\partial \bar{u}_r}{\partial r} = -\frac{\partial \bar{p}}{\partial r}, \tag{C1}$$

which gives for the mean radial velocity the following expression:

$$\bar{u}_r = \sqrt{-2 \int_0^\infty \frac{1}{\bar{\rho}} \frac{\partial \bar{p}}{\partial r} \mathrm{d}r}. \tag{C2}$$

The radial derivative is computed using a centred finite-difference method. The radial profile of the mean radial velocity normalised by the jet Mach number downstream of the shock is reported in figure 16. We note that $\bar{u}_r \neq 0$ in the shear-layer region with a peak for $r = 0.5$. Nevertheless, since the maximum value is approximately 10 % of the jet velocity, we may assert that the jet is slowly diverging downstream of the shock, but this feature does not affect the evaluation of the reflection coefficient given that both the reflection and transmission mechanisms happen locally and are not influenced by the flow evolution far away from the shock.

Appendix D. Relevance of the near-sonic, downstream-travelling acoustic modes

As outlined in Mancinelli *et al.* (2022), propagative, downstream-travelling acoustic modes in the vicinity of the sonic line cannot be described using the confined V-S model due to numerical issues in the root-finder algorithm when searching for zeros of the dispersion relation. Furthermore, the resolution of the acoustic branch close to the sonic line is function of the distance of the wall boundary r_{MAX}, as exemplified in figure 17, which shows the maximum value of the acoustic eigenvalue of the propagative, downstream-travelling branch as a function of r_{MAX}. The resolution in the vicinity of the sonic line deteriorates for increasing r_{MAX}, thus bringing into question the reliability of the results obtained using the V-S. To prove the little relevance of near-sonic, downstream-travelling acoustic modes in the determination of the reflection coefficient we consider the F-T model and compute R both including and excluding near-sonic modes.
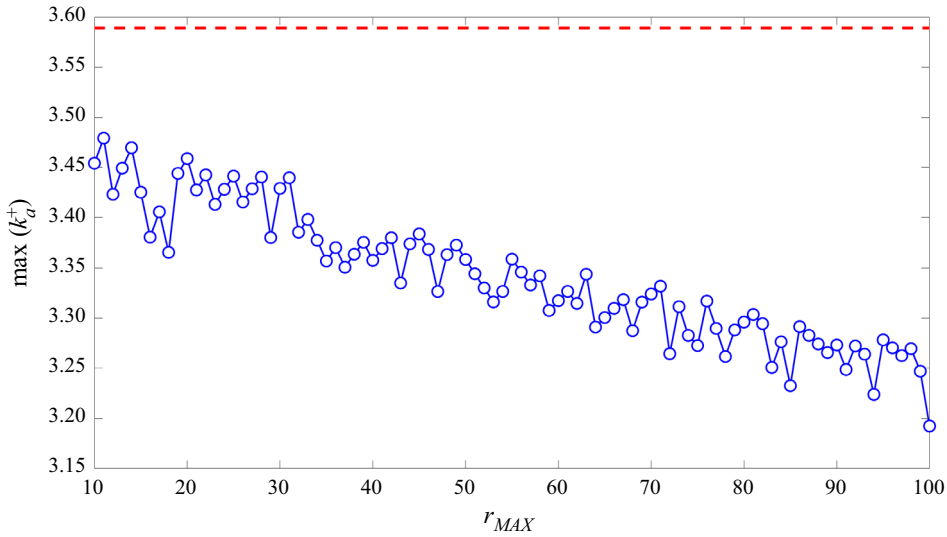
954 A9-26

Figure 17. Maximum eigenvalue of the propagative, downstream-travelling acoustic branch as a function of the wall distance using the confined V-S model. Flow conditions are the same reported in figure 5 downstream of the shock. Blue ○ represent the eigenvalue, dashed red line the position of the sonic line.
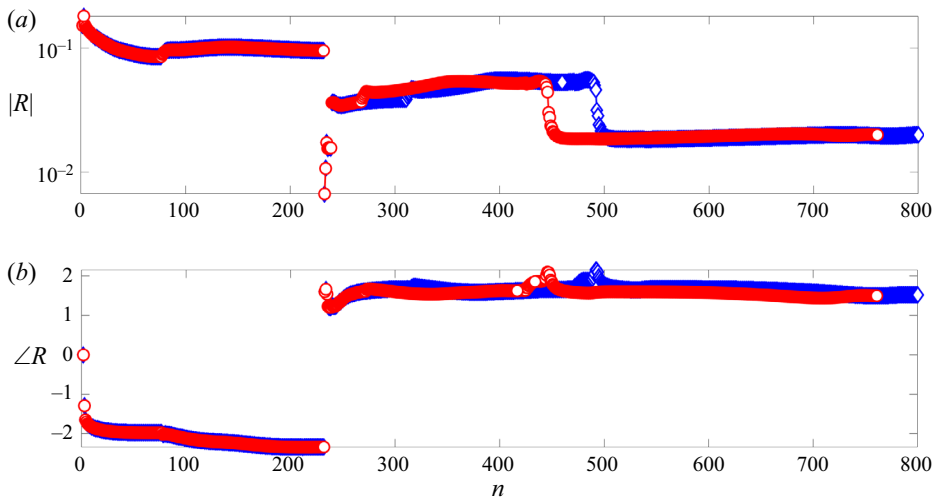

Figure 18. Evolution of the reflection coefficient as a function of the number of modes considered using the F-T model: blue ◇ refer to results obtained including near-sonic, downstream-travelling acoustic modes, red ○ refer to results obtained artificially removing near-sonic acoustic modes ($k_{a_{MAX}}^+ = 3.2$). (*a*) Amplitude, (*b*) phase.

The comparison in figure 18 shows no discrepancy in terms of both amplitude and phase when near-sonic acoustic modes are artificially removed from the reduced basis of the transmitted modes, thus suggesting the small influence of these modes in the reflection coefficient calculation and confirming the reliability of the results obtained using the V-S. To further support this assertion, we finally show in figure 19 the variation of the objective function F, the reflection-coefficient amplitude and phase as a function of r_{MAX} when using the V-S to describe the jet dynamics. The variation is relative to the results obtained
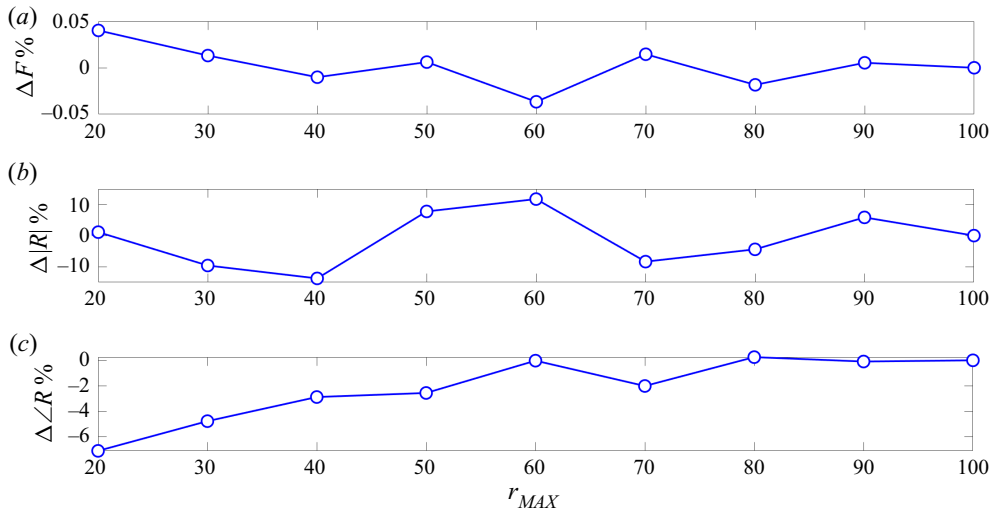
Figure 19. Variation of the objective function, amplitude and phase of the reflection coefficient as a function of the wall distance using the confined V-S model. Variations are relative to the results obtained for $r_{MAX} = 100$ presented throughout the manuscript. (*a*) Objective function, (*b*) reflection-coefficient amplitude, (*c*) reflection-coefficient phase.

using $r_{MAX} = 100$ and presented throughout the manuscript. We observe variation lower than 0.1 % for the objective function and of the order of 10 % and 7 % at maximum for the reflection-coefficient amplitude and phase, respectively. These variations are considered acceptable especially given that, as outlined by Mancinelli *et al.* (2022), the change of r_{MAX} implies a change of the discretisation of the acoustic branch and, hence, of the number of modes considered in the calculation of the reflection coefficient.

REFERENCES

ANDREOPOULOS, Y., AGUI, J.H. & BRIASSULIS, G. 2000 Shock wave–turbulence interactions. *Annu. Rev. Fluid Mech.* **32** (1), 309–345.

BERS, A. 1983 Space-time evolution of plasma instabilities-absolute and convective. In *Basic Plasma Physics*, vol. 1. International Nuclear Information System.

BOGEY, C. & GOJON, R. 2017 Feedback loop and upwind-propagating waves in ideally expanded supersonic impinging round jets. *J. Fluid Mech.* **823**, 562–591.

BRIGGS, R.J. 1964 *Electron-Stream Interaction with Plasmas*. MIT Press.

BUTTSWORTH, D.R. 1996 Interaction of oblique shock waves and planar mixing regions. *J. Fluid Mech.* **306**, 43–57.

CAVALIERI, A.V.G., JORDAN, P. & LESSHAFFT, L. 2019 Wave-packet models for jet dynamics and sound radiation. *Appl. Mech. Rev.* **71** (2), 020802.

CHEN, C.H. & DONZIS, D.A. 2019 Shock–turbulence interactions at high turbulence intensities. *J. Fluid Mech.* **870**, 813–847.

CHU, B.T. 1965 On the energy transfer to small disturbances in fluid flow (part I). *Acta Mechanica* **1** (3), 215–234.

CLEMENS, N.T. & NARAYANASWAMY, V. 2014 Low-frequency unsteadiness of shock wave/turbulent boundary layer interactions. *Annu. Rev. Fluid Mech.* **46**, 469–492.

DAI, X. 2020 Flow–acoustic resonance in a cavity covered by a perforated plate. *J. Fluid Mech.* **884**, A4.

DAI, X. 2021 Total reflection of two guided waves for embedded trapped modes. *AIAA J.* **59** (1), 131–139.

DELERY, J.M. 1983 Experimental investigation of turbulence properties in transonic shock/boundary-layer interactions. *AIAA J.* **21** (2), 180–185.

DOLLING, D.S. 2001 Fifty years of shock-wave/boundary-layer interaction research: what next? *AIAA J.* **39** (8), 1517–1531.

DURAN, I. & MOREAU, S. 2013 Solution of the quasi-one-dimensional linearized Euler equations using flow invariants and the magnus expansion. *J. Fluid Mech.* **723**, 190–231.

DURAN, I. & MORGANS, A.S. 2015 On the reflection and transmission of circumferential waves through nozzles. *J. Fluid Mech.* **773**, 137–153.

EDGINGTON-MITCHELL, D. 2019 Aeroacoustic resonance and self-excitation in screeching and impinging supersonic jets–a review. *Intl J. Aeroacoust.* **18** (2–3), 118–188.

EDGINGTON-MITCHELL, D., JAUNET, V., JORDAN, P., TOWNE, A., SORIA, J. & HONNERY, D. 2018 Upstream-travelling acoustic jet modes as a closure mechanism for screech. *J. Fluid Mech.* **855**, R1.

EDGINGTON-MITCHELL, D., WANG, T., NOGUEIRA, P.A.S., SCHMIDT, O., JAUNET, V., DUKE, D., JORDAN, P. & TOWNE, A. 2021*a* Waves in screeching jets. *J. Fluid Mech.* **913**, A7.

EDGINGTON-MITCHELL, D., WEIGHTMAN, J., LOCK, S., KIRBY, R., NAIR, V., SORIA, J. & HONNERY, D. 2021*b* The generation of screech tones by shock leakage. *J. Fluid Mech.* **908**, A46.

GABARD, G. & ASTLEY, R.J. 2008 A computational mode-matching approach for sound propagation in three-dimensional ducts with flow. *J. Sound Vib.* **315** (4–5), 1103–1124.

GÉNIN, F. & MENON, S. 2010 Studies of shock/turbulent shear layer interaction using large-eddy simulation. *Comput. Fluids* **39** (5), 800–819.

GOH, C.S. & MORGANS, A.S. 2011 Phase prediction of the response of choked nozzles to entropy and acoustic disturbances. *J. Sound Vib.* **330** (21), 5184–5198.

GOJON, R., BOGEY, C. & MIHAESCU, M. 2018 Oscillation modes in screeching jets. *AIAA J.* **56** (7), 1–7.

HANIFI, A., SCHMID, P.J. & HENNINGSON, D.S. 1996 Transient growth in compressible boundary layer flow. *Phys. Fluids* **8** (3), 826–837.

JORDAN, P. & COLONIUS, T. 2013 Wave packets and turbulent jet noise. *Annu. Rev. Fluid Mech.* **45**, 173–195.

KITAMURA, T., NAGATA, K., SAKAI, Y., SASOH, A. & ITO, Y. 2016 Rapid distortion theory analysis on the interaction between homogeneous turbulence and a planar shock wave. *J. Fluid Mech.* **802**, 108–146.

LELE, S.K. 2005 Phased array models of shock-cell noise sources. In *11th AIAA/CEAS Aeroacoustics Conference. AIAA Paper* 2005-2841.

LESSEN, M., FOX, J.A. & ZIEN, H.M. 1965 On the inviscid stability of the laminar mixing of two parallel streams of a compressible fluid. *J. Fluid Mech.* **23** (2), 355–367.

LESSHAFFT, L. & HUERRE, P. 2007 Linear impulse response in hot round jets. *Phys. Fluids* **19** (2), 024102.

LESSHAFFT, L., SEMERARO, O., JAUNET, V., CAVALIERI, A.V.G. & JORDAN, P. 2019 Resolvent-based modeling of coherent wave packets in a turbulent jet. *Phys. Rev. Fluids* **4** (6), 063901.

LEVENBERG, K. 1944 A method for the solution of certain non-linear problems in least squares. *Q. Appl. Maths* **2** (2), 164–168.

MAHESH, K., LEE, S., LELE, S.K. & MOIN, P. 1995 The interaction of an isotropic field of acoustic waves with a shock wave. *J. Fluid Mech.* **300**, 383–407.

MAHESH, K., LELE, S.K. & MOIN, P. 1997 The influence of entropy fluctuations on the interaction of turbulence with a shock wave. *J. Fluid Mech.* **334**, 353–379.

MANCINELLI, M., JAUNET, V., JORDAN, P. & TOWNE, A. 2019*a* Screech-tone prediction using upstream-travelling jet modes. *Exp. Fluids* **60** (1), 22.

MANCINELLI, M., JAUNET, V., JORDAN, P. & TOWNE, A. 2021 A complex-valued resonance model for axisymmetric screech tones in supersonic jets. *J. Fluid Mech.* **928**, A32.

MANCINELLI, M., JAUNET, V., JORDAN, P., TOWNE, A. & GIRARD, S. 2019*b* Reflection coefficients and screech-tone prediction in supersonic jets. In *25th AIAA/CEAS Aeroacoustics Conference. AIAA Paper* 2019-2522.

MANCINELLI, M., MARTINI, E., JAUNET, V. & JORDAN, P. 2022 Including acoustic modes in the vortex-sheet eigenbasis of a jet. *J. Acoust. Soc. Am.* **151** (2), 852–860.

MARBLE, F.E. & CANDEL, S.M. 1977 Acoustic disturbance from gas non-uniformities convected through a nozzle. *J. Sound Vib.* **55** (2), 225–243.

MARQUARDT, D.W. 1963 An algorithm for least-squares estimation of nonlinear parameters. *SIAM J. Appl. Maths* **11** (2), 431–441.

MARTINI, E., CAVALIERI, A.V.G. & JORDAN, P. 2019 Acoustic modes in jet and wake stability. *J. Fluid Mech.* **867**, 804–834.

MERCIER, B., CASTELAIN, T. & BAILLY, C. 2017 Experimental characterisation of the screech feedback loop in underexpanded round jets. *J. Fluid Mech.* **824**, 202–229.

MICHALKE, A. 1970 A note on the spatial jet-lnstability of the compressible cylindrical vortex sheet. *Tech. Rep.* DLR.

MICHALKE, A. 1984 Survey on jet instability theory. *Prog. Aerosp. Sci.* **21**, 159–199.

MOORE, F.K. 1954 Unsteady oblique interaction of a shock wave with a plane disturbance. NACA Tech. Rep. 1165.

NOGUEIRA, P.A.S., CAVALIERI, A.V.G., JORDAN, P. & JAUNET, V. 2019 Large-scale streaky structures in turbulent jets. *J. Fluid Mech.* **873**, 211–237.

NOGUEIRA, P.A.S., JAUNET, V., MANCINELLI, M., JORDAN, P. & EDGINGTON-MITCHELL, D. 2022 Closure mechanism of the A1 and A2 modes in jet screech. *J. Fluid Mech.* **936**, A10.

PANDA, J. 1999 An experimental investigation of screech noise generation. *J. Fluid Mech.* **378**, 71–96.

POWELL, A. 1953 On the mechanism of choked jet noise. In *Proc. Phys. Soc. London, Sec. B*, vol. 66, p. 1039.

POWELL, A., UMEDA, Y. & ISHII, R. 1992 Observations of the oscillation modes of choked circular jets. *J. Acoust. Soc. Am.* **92** (5), 2823–2836.

RAMAN, G. 1999 Supersonic jet screech: half-century from Powell to the present. *J. Sound Vib.* **225** (3), 543–571.

RIBNER, H.S. 1954 Convection of a pattern of vorticity through a shock wave. NACA Tech. Rep. 1164.

RIBNER, H.S. 1955 Shock-turbulence interaction and the generation of noise. NACA Tech. Rep. 1233.

ROSSITER, J.E. 1964 Wind-tunnel experiments on the flow over rectangular cavities at subsonic and transonic speeds. *Tech. Rep.* 3438. Royal Aircraft Establishment.

ROWLEY, C.W., COLONIUS, T. & BASU, A.J. 2002 On self-sustained oscillations in two-dimensional compressible flow over rectangular cavities. *J. Fluid Mech.* **455**, 315–346.

SCHMID, P.J. & HENNINGSON, D.S. 2001 *Stability and Transition in Shear Flows*, 1st edn. Applied Mathematical Sciences, vol. 142. Springer.

SCHMIDT, O.T., TOWNE, A., COLONIUS, T., CAVALIERI, A.V.G., JORDAN, P. & BRÈS, G.A. 2017 Wavepackets and trapped acoustic modes in a turbulent jet: coherent structure eduction and global stability. *J. Fluid Mech.* **825**, 1153–1181.

SHEN, H. & TAM, C.K.W. 2002 Three-dimensional numerical simulation of the jet screech phenomenon. *AIAA J.* **40** (1), 33–41.

STOW, S.R., DOWLING, A.P. & HYNES, T.P. 2002 Reflection of circumferential modes in a choked nozzle. *J. Fluid Mech.* **467**, 215–239.

SUZUKI, T. & LELE, S.K. 2003 Shock leakage through an unsteady vortex-laden mixing layer: application to jet screech. *J. Fluid Mech.* **490**, 139–167.

TAM, C.K.W. & AHUJA, K.K. 1990 Theoretical model of discrete tone generation by impinging jets. *J. Fluid Mech.* **214**, 67–87.

TAM, C.K.W. & HU, F.Q. 1989 On the three families of instability waves of high-speed jets. *J. Fluid Mech.* **201**, 447–483.

TAM, C.K.W., SEINER, J.M. & YU, J.C. 1986 Proposed relationship between broadband shock associated noise and screech tones. *J. Sound Vib.* **110** (2), 309–321.

TAM, C.K.W. & TANNA, H.K. 1982 Shock associated noise of supersonic jets from convergent-divergent nozzles. *J. Sound Vib.* **81** (3), 337–358.

TANNA, H.K. 1977 An experimental study of jet noise. Part II. Shock associated noise. *J. Sound Vib.* **50** (3), 429–444.

TISSOT, G., ZHANG, M., LAJÚS, F.C., CAVALIERI, A.V.G. & JORDAN, P. 2017 Sensitivity of wavepackets in jets to nonlinear effects: the role of the critical layer. *J. Fluid Mech.* **811**, 95–137.

TOWNE, A., CAVALIERI, A.V.G., JORDAN, P., COLONIUS, T., SCHMIDT, O., JAUNET, V. & BRÈS, G.A. 2017 Acoustic resonance in the potential core of subsonic jets. *J. Fluid Mech.* **825**, 1113–1152.

TOWNE, A., SCHMIDT, O.T. & COLONIUS, T. 2018 Spectral proper orthogonal decomposition and its relationship to dynamic mode decomposition and resolvent analysis. *J. Fluid Mech.* **847**, 821–867.

YANG, J., KUBOTA, T. & ZUKOSKI, E.E. 1993 Applications of shock-induced mixing to supersonic combustion. *AIAA J.* **31** (5), 854–862.